

Check for updates

Bioinspired Adaptive Sensors: A Review on Current Developments in Theory and Application

Guodong Gong, You Zhou, Qingxiu Li, Wenyu Zhao, Sunyingyue Geng, Hangfei Li, Yan-Bing Leng, Shirui Zhu, Guanglong Ding, Yongbiao Zhai, Ziyu Lv, Ye Zhou, and Su-Ting Han*

The human perception system features many dynamic functional mechanisms that efficiently process the large amount of sensory information available in the surrounding environment. In this system, sensory adaptation operates as a core mechanism that seamlessly filters familiar and inconsequential external stimuli at sensory endpoints. Such adaptive filtering minimizes redundant data movement between sensory terminals and cortical processing units and contributes to a lower communication bandwidth requirement and lower energy consumption at the system level. Recreating the behavior of sensory adaptation using electronic devices has garnered significant research interest owing to its promising prospects in next-generation intelligent perception platforms. Herein, the recent progress in bioinspired adaptive device engineering is systematically examined, and its valuable applications in electronic skins, wearable electronics, and machine vision are highlighted. The rapid development of bioinspired adaptive sensors can be attributed not only to the recent advances in emerging neuromorphic electronic elements, including piezoelectric and triboelectric sensors, memristive devices, and neuromorphic transistors, but also to the improved understanding of biological sensory adaptation. Existing challenges hindering device performance optimization, multimodal adaptive sensor development, and system-level integration are also discussed, providing insights for the development of high-performance neuromorphic sensing systems.

1. Introduction

The Internet of Things (IoT) landscape can be characterized by a large number sensory nodes, which are growing rapidly and are predicted to reach 125 billion by 2030.[1,2] These sensors can effectively record information about the surrounding environment; however, they also generate a large amount of redundant data.[3-7] In conventional sensory computing systems, the sensing and processing units are separated in the physical space. [8-11] Typically, the analog sensory output is first converted into a digital format and then temporarily stored in memory before being further relayed to the processing unit.[12-15] The massive and mostly uninformative data passing through the sensor-memoryprocessor signal chain may lead to significant latency and power consumption.[16-18] This pedantic and power-consuming nature significantly limits the application of conventional sensory computing systems in data-intensive and delay-sensitive fields such as wearable electronics, interactive robotics, and real-time video analysis.[19,20]

G. Gong, Y. Zhou, Q. Li, W. Zhao Institute of Microscale Optoelectronics Shenzhen University Shenzhen 518060, P. R. China G. Gong, S. Geng, H. Li, G. Ding, Y. Zhai, Z. Lv College of Electronics and Information Engineering Shenzhen University Shenzhen 518060, P. R. China

The ORCID identification number(s) for the author(s) of this article can be found under https://doi.org/10.1002/adma.202505420

© 2025 The Author(s). Advanced Materials published by Wiley-VCH GmbH. This is an open access article under the terms of the Creative Commons Attribution-NonCommercial License, which permits use, distribution and reproduction in any medium, provided the original work is properly cited and is not used for commercial purposes.

DOI: 10.1002/adma.202505420

G. Ding State Key Laboratory of Radio Frequency Heterogeneous Integration Shenzhen University Shenzhen 518060, P. R. China

Institute for Advanced Study Shenzhen University Shenzhen 518060, P. R. China Y.-B. Leng, S. Zhu, S.-T. Han

Department of Applied Biology and Chemical Technology and Research Institute for Smart Energy

The Hong Kong Polytechnic University, Hung Hom Kowloon, Hong Kong 999077, P. R. China E-mail: suting.han@polyu.edu.hk

15214095, 0, Downloaded from https://advanced.onlinelibrary.wiley.com/doi/10.1002/adma.202505420 by HONG KONG POLYTECHNIC UNIVERSITY HU NG HOM, Wiley Online Library on [2609/2025]. See the Terms and Conditions (https://onlinelibrary.wiley.com/doi/10.1002/adma.202505420 by HONG KONG POLYTECHNIC UNIVERSITY HU NG HOM, Wiley Online Library on [2609/2025]. See the Terms and Conditions (https://onlinelibrary.wiley.com/doi/10.1002/adma.202505420 by HONG KONG POLYTECHNIC UNIVERSITY HU NG HOM, Wiley Online Library on [2609/2025]. See the Terms and Conditions (https://onlinelibrary.wiley.com/doi/10.1002/adma.202505420 by HONG KONG POLYTECHNIC UNIVERSITY HU NG HOM, Wiley Online Library on [2609/2025]. See the Terms and Conditions (https://onlinelibrary.wiley.com/doi/10.1002/adma.202505420 by HONG KONG POLYTECHNIC UNIVERSITY HU NG HOM, Wiley Online Library on [2609/2025]. See the Terms and Conditions (https://onlinelibrary.wiley.com/doi/10.1002/adma.202505420 by HONG KONG POLYTECHNIC UNIVERSITY HU NG HOM, Wiley Online Library on [2609/2025]. See the Terms and Conditions (https://onlinelibrary.wiley.com/doi/10.1002/adma.202505420 by HONG KONG POLYTECHNIC UNIVERSITY HU NG HOM, Wiley Online Library on [2609/2025]. See the Terms and Conditions (https://onlinelibrary.wiley.com/doi/10.1002/adma.202505420 by HONG KONG POLYTECHNIC UNIVERSITY HU NG HOM. Wiley Online Library on [2609/2025]. See the Terms and Conditions (https://onlinelibrary.wiley.com/doi/10.1002/adma.202505420 by HONG KONG POLYTECHNIC UNIVERSITY HU NG HOM. Wiley Online Library on [2609/2025]. See the Terms and Conditions (https://onlinelibrary.wiley.com/doi/10.1004/adma.202505420 by HONG KONG POLYTECHNIC UNIVERSITY HU NG HOM. Wiley Online Library on [2609/2025]. See the Terms and Conditions (https://onlinelibrary.wiley.com/doi/10.1004/adma.202505420 by HONG KONG POLYTECHNIC UNIVERSITY HU NG HOM. Wiley Online Library on [2609/2025]. See the Terms and Conditions (https://onlinelibrary.wiley.com/doi/10.1004/adma.202505420 by HONG KONG POLYTECHNIC UNIVERSITY HU NG HOM.

com/terms-and-conditions) on Wiley Online Library for rules of use; OA articles are governed by the applicable Creative Commons L

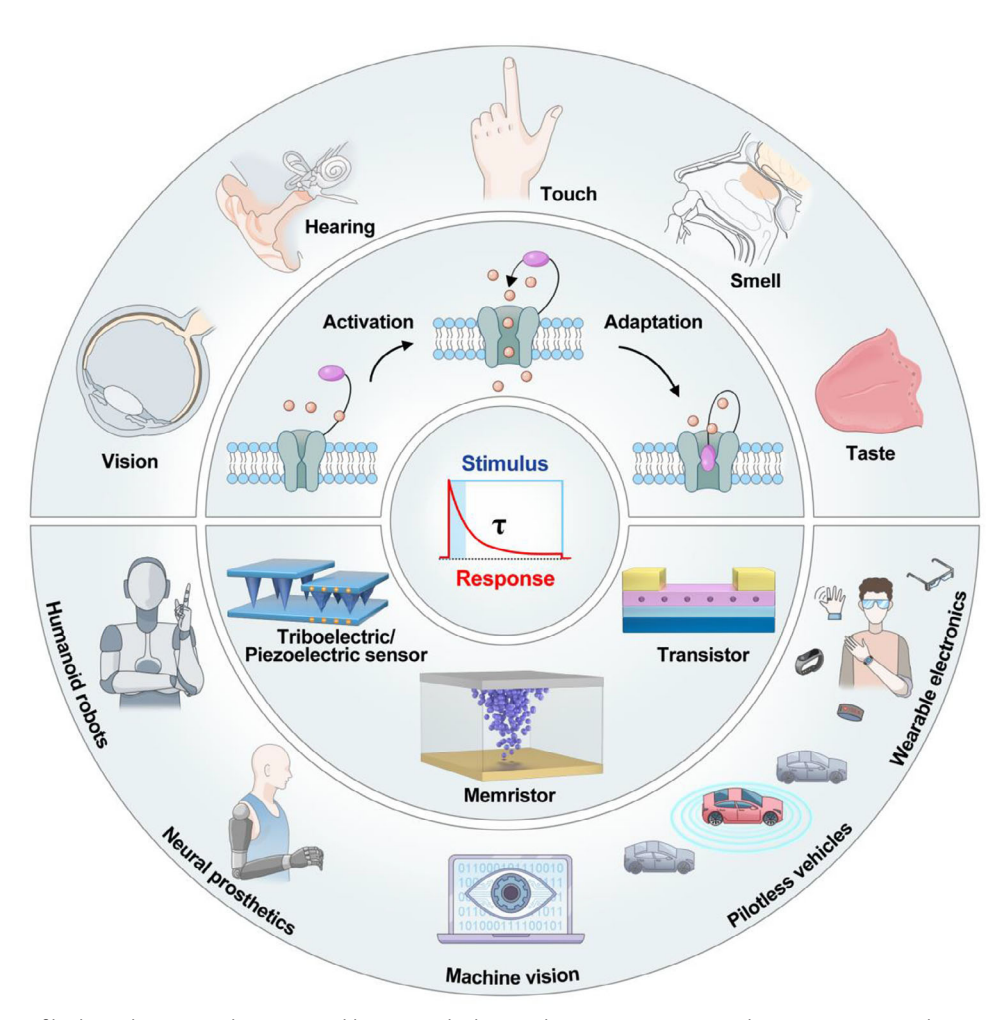


Figure 1. Schematic of biological sensory adaptation and bioinspired adaptive devices. Top: Sensory adaptation process in bio-systems and the classic five senses—vision, hearing, touch, smell, and taste—all of which can be characterized by rapid adaptation. Bottom: Bioinspired adaptive devices and their applications.

Unlike conventional sensors with fixed response characteristics, human sensory neurons can dynamically adjust their responsiveness depending on the environmental conditions.^[21–25] This process, termed sensory adaptation, represents a ubiquitous feature of sensory transduction, enabling sensory cells to simultaneously register, integrate, and preprocess environmental signals prior to transmitting them to the central processing center through neural pathways.^[26] More precisely, sensory adaptation permits sensory neurons to flexibly modulate their input response dynamics based on the frequency, intensity, and temporal patterns of external stimuli.[27,28] A common adjustment involves reducing the responsiveness of perception systems to the continuous presence of stimuli or background signals.^[29,30] This distinctive capability enables an effective strategy for neural encoding while simultaneously eliminating routine or unimportant environmental elements through seamless filtration.[31] Consequently, substantial quantities of nonessential data captured by various sensory receptors are filtered during the early processing stages, thereby significantly reducing the burden of transmitting data that lack informational value.[32,33] Furthermore, sensory adaptation enables the amplification of weak input signals while preventing the response to strong signals from saturating.^[34] Such active regulation not only facilitates the extension of the range of input perceived by biological sensory systems but also significantly decreases power consumption with an increase in stimulus intensity.^[35,36]

Inspired by the low-power and high-efficiency characteristics of biological sensory adaptation, researchers have made extensive efforts toward creating artificial adaptive sensors using semiconductor devices and circuits.[37,38] Historically, silicon-based complementary metal-oxide-semiconductor (CMOS) circuits were explored to mimic the functions of sensory adaptation. [39,40] However, given the lack of an intrinsic biological resemblance of CMOS devices, dozens of transistors and capacitors are typically employed to realize environmentally adaptable characteristics; these devices are bulky, energy-hungry, and unfavorable for miniaturization.^[41] In recent years, several types of emerging devices that can naturally exhibit rich neural behaviors have been successfully developed to replicate sensory adaptation processes, such as piezoelectric and triboelectric sensors, [42-45] memristors, [46–48] and neuromorphic transistors [49–53] (**Figure 1**). Adaptive sensors based on these devices have advantages such as

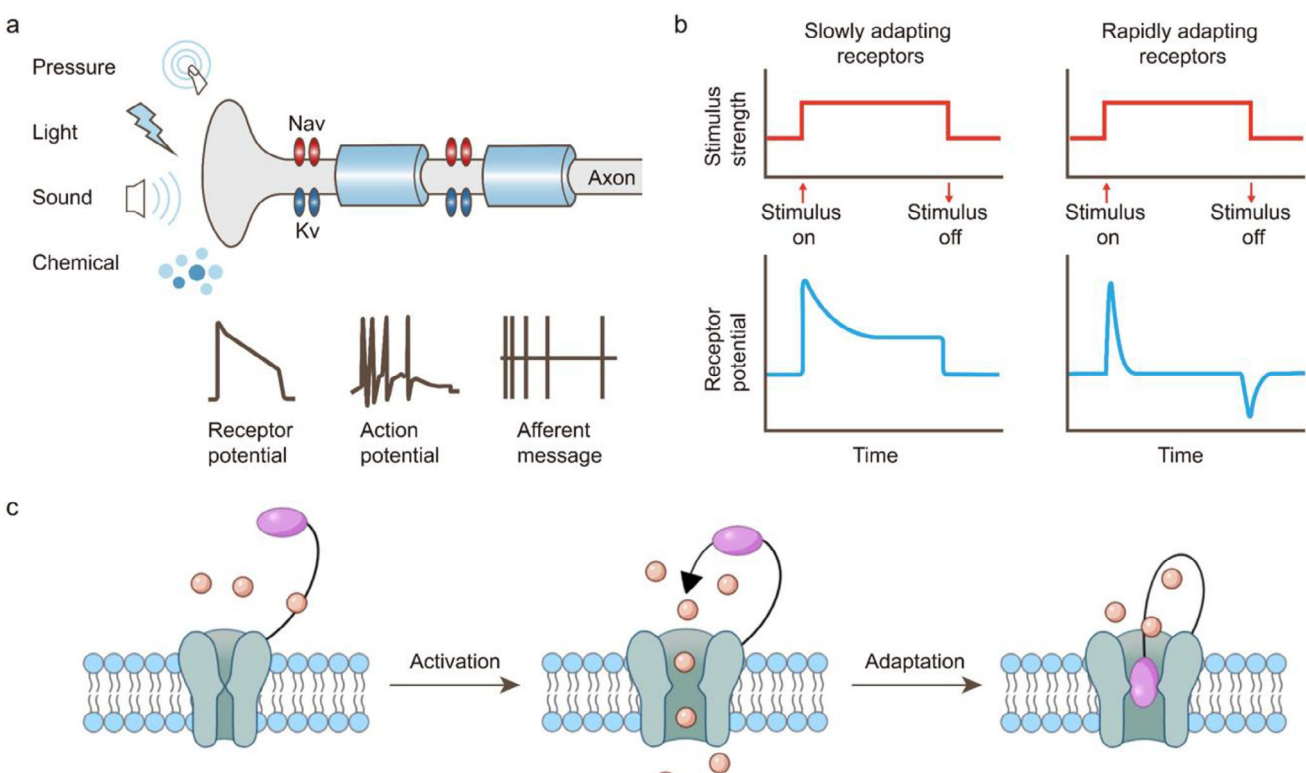


Figure 2. Schematic of sensory transduction and adaptation: a) Sensory neurons transform the energy of external stimulus into receptor potential through sensory transduction and further convert it into action potential at the axon end of afferent nerve; Adapted with permission.^[55] Copyright 2011, Springer Nature. b) Responses of slowly adapting receptors and rapidly adapting receptors. c) Sensory adaptation process in bio-systems. Sensory adaptation is dominated by the gating dynamics of transduction-related ion channels in the receptor membrane.

structural simplicity, compact dimensions, energy-efficient operation, and high compatibility with integrated technologies.

Herein, we summarize recent significant advances in bioin-spired adaptive sensors from the perspectives of both device design and novel applications. First, we introduce the biological principles of sensory adaptation as a neurophysiological basis for bioinspired adaptive sensors. The representative progress made in this field is then discussed in terms of various implementation strategies, including piezoelectric and triboelectric sensors, memristive devices, and neuromorphic transistors. Furthermore, we explore the fascinating applications of bioinspired adaptive sensors in different scenarios, such as electronic skins, wearable electronics, and machine vision. Finally, existing challenges hindering their broader application are discussed in detail, providing valuable perspectives for advancing high-performance neuromorphic sensing systems.

2. Biological Principles of Sensory Adaptation

Sensory systems provide important information for human survival and well-being during interactions with the external environment (Figure 2a). Various peripheral sensory receptors are responsible for detecting environmental stimuli and transmitting this information to the central nervous system.^[54] These receptors transform the energy of external stimuli into electrical signals, namely, receptor potentials, through a process called sen-

sory transduction. Sensory transduction occurs in the receptive endings of sensory neurons, involving the opening and closing of membrane ion channels, along with the subsequent transmembrane transport of associated ions. The resulting receptor potential is further converted into a train of action potentials with variable frequency and duration at the axon end of the afferent nerve and then transmitted to the central nervous system.^[55]

Sensory adaptation occurs during sensory transduction, and it refers to the phenomenon in which the magnitude of the receptor potential adapts to a lower level when a constant stimulus is applied to the sensory cell for some duration. Most sensory receptors adapt to external stimulus over time. Based on their adaptation speed, they fall into two broad categories: slowly adapting and rapidly adapting receptors (Figure 2b). [56-58] Slowly adapting receptors, also known as tonic receptors, exhibit little adaptation; that is, they maintain their responses well over time. Therefore, they can better encode the duration and intensity of a stimulus. Examples of tonic receptors include Merkel cells in the skin, which are responsible for the perception of texture and form, and nociceptors distributed throughout the body, which respond to potential threats or injurious stimuli. Rapidly adapting receptors, also known as phasic receptors, respond well at the beginning of a stimulus and then adapt quickly. Some specific mechanoreceptors in the skin also show a second, smaller response, called "off response," as the stimulus is removed. Phasic receptors are specialized for detecting the onset and offset of a stimulus, and

ADVANCED MATERIALS

www.advmat.de

changes in stimulus intensity. The five senses—vision, hearing, touch, smell, and taste—are characterized by rapid adaptation. These senses, which are ubiquitous in our daily life, are responsible for various inherent phenomena, including our accommodation of ambient light conditions and the sound of city traffic, the disappearing feeling of clothes on the body, and the fading perception of intense odors (bitter coffee).

In human perception systems, sensory adaptation is dominated by the gating dynamics of transduction-related ion channels in the receptor membrane (Figure 2c).[59,60] During sustained stimulation, ion channels are first activated and then gradually deactivated via a feedback regulation mechanism. After turning off the stimulus, they quickly return from the inactivated state to the initial state. Sensory adaptation has been formed through constant interaction with the external environment during the evolutionary process and has vital biological significance.[61-64] First, sensory adaptation filters out temporally and spatially repetitive, uninformative signal components and allows the perception system to adapt to the ambient environment.[26,31] Such adaptive filtering minimizes redundant data exchange between sensory terminals and cortical processing units, significantly improving energy efficiency and reducing communication bandwidth requirements. Second, sensory adaptation improves the sensitivity to stimulus changes at the cost of reduced fidelity under steady-state conditions.[31,65] This ability permits sensory systems to prioritize the processing of salient features in the environment, despite the huge amount of information we receive from the surrounding world. Third, sensory adaptation allows for significant amplification of weak input signals while avoiding the saturation of responses to strong stimuli.[27,35] This is achieved by dynamically tuning sensitivity and fitness based on the current stimulus range in each environment. Such active regulation significantly extends the input range to which the biological sensory system responds and plays a crucial role in maintaining steady perception in the presence of changes in the stimulus and context.

2.1. Biological Tactile Adaptation

Mechanotransduction, which is the transformation of a mechanical stimulus into a biological response, plays a vital role in mediating our interactions with the physical world. Mechanoreceptors are the most widespread in the human perception system and are distributed throughout the body. [65,66] These sensory neurons function as selective peripheral coding units that are specifically designed to gather data on the diverse characteristics of mechanical forces and provide a neurological representation of the physical environment to the central nervous system. The skin, our body's largest organ, covering a surface area of $\approx 2 \text{ m}^2$, houses humanity's most famous mechanoreceptors. [66,67] These cutaneous sensory receptors can detect multiple forms of mechanical stimuli such as light touch, vibratory cues, object shape, surface texture, and painful pressure. This wide range of stimuli is matched by a diverse array of functionally distinct mechanoreceptor subtypes that respond to cutaneous deformation or motion in distinct manners.

Tactile sensations in the human hand are mediated by four types of mechanoreceptors: Merkel cells, Ruffini corpuscles,

Meissner corpuscles, and Pacinian corpuscles (Figure 3). [68] Two of these receptor cells, namely, Merkel cells and Ruffini corpuscles, exhibit a slowly adapting behavior and produce a sustained signal in response to a steady pressure on the skin. The other two, namely, Meissner and Pacinian corpuscles, exhibit rapidly adapting behaviors that respond selectively to dynamic forces or vibrations, but not to steady pressure. [61,69] In addition, the four types of mechanoreceptors vary in morphology, location within the skin, innervation pattern, receptive field size, and perceptual function. [68] Merkel cells and Meissner corpuscles are both small receptor cells located in the superficial layer of the skin, 0.5 to 1.0 mm below the cutaneous surface. The afferent nerve fiber innervates these mechanosensory neuron branches at its terminal such that each fiber innervates multiple adjacent sensory neurons. The Ruffini and Pacinian corpuscles are larger and fewer in number than the first two receptor cells. These are located deep within the skin and in the subcutaneous tissues. The afferent nerve fibers that innervate these mechanosensory neurons terminate without branching; that is, each sensory neuron is innervated by a single nerve fiber, and each nerve fiber only receives the output signal of a single sensory neuron. The receptive field of mechanoreceptors refers to a limited area of the skin, and stimulation of this area elicits a response from the mechanoreceptors. The size of the receptive field is related to the location and distribution of the mechanosensory neurons. Specifically, tactile neurons near the surface of the skin have a smaller receptive field than those in the deeper layers.

These structural differences endow the four mechanoreceptor types with various perceptual functions. Merkel cells detect cutaneous indentation depth and have the highest spatial resolution among all tactile neurons.^[70,71] They are particularly sensitive to object edges and corners, which are responsible for distinguishing shapes and textures. A blind person uses this ability to read Braille at a speed of 100 words per minute. Ruffini corpuscles respond more vigorously to cutaneous stretching than to indentation. [61,72] They are primarily responsible for measuring the direction of object motion according to the stretching pattern. Meissner corpuscles transmit information regarding dynamic skin deformation and low-frequency vibration (5-50 Hz).[73,74] They play an important role in monitoring the slippage of objects humans handle, enabling us to appropriately adjust the grip. Pacinian corpuscles are mechanosensory neurons that are most sensitive to skin motion and are capable of registering mechanical motion in the nanometer range. [70,75] This unique ability contributes to the detection of high-frequency vibrations (up to 400 Hz) produced by objects grasped by the hand. The ensemble output of these mechanoreceptors provides information to the brain regarding the stimulus location, amplitude, object size, shape, texture, and how these features vary over time.^[71] The time latency between an external stimulus and the corresponding neural activation in the brain typically spans several tens of milliseconds.[61]

2.2. Biological Visual Adaptation

Visual perception serves as the predominant channel through which humans receive information from the outside world and provides important information for distinguishing the size,

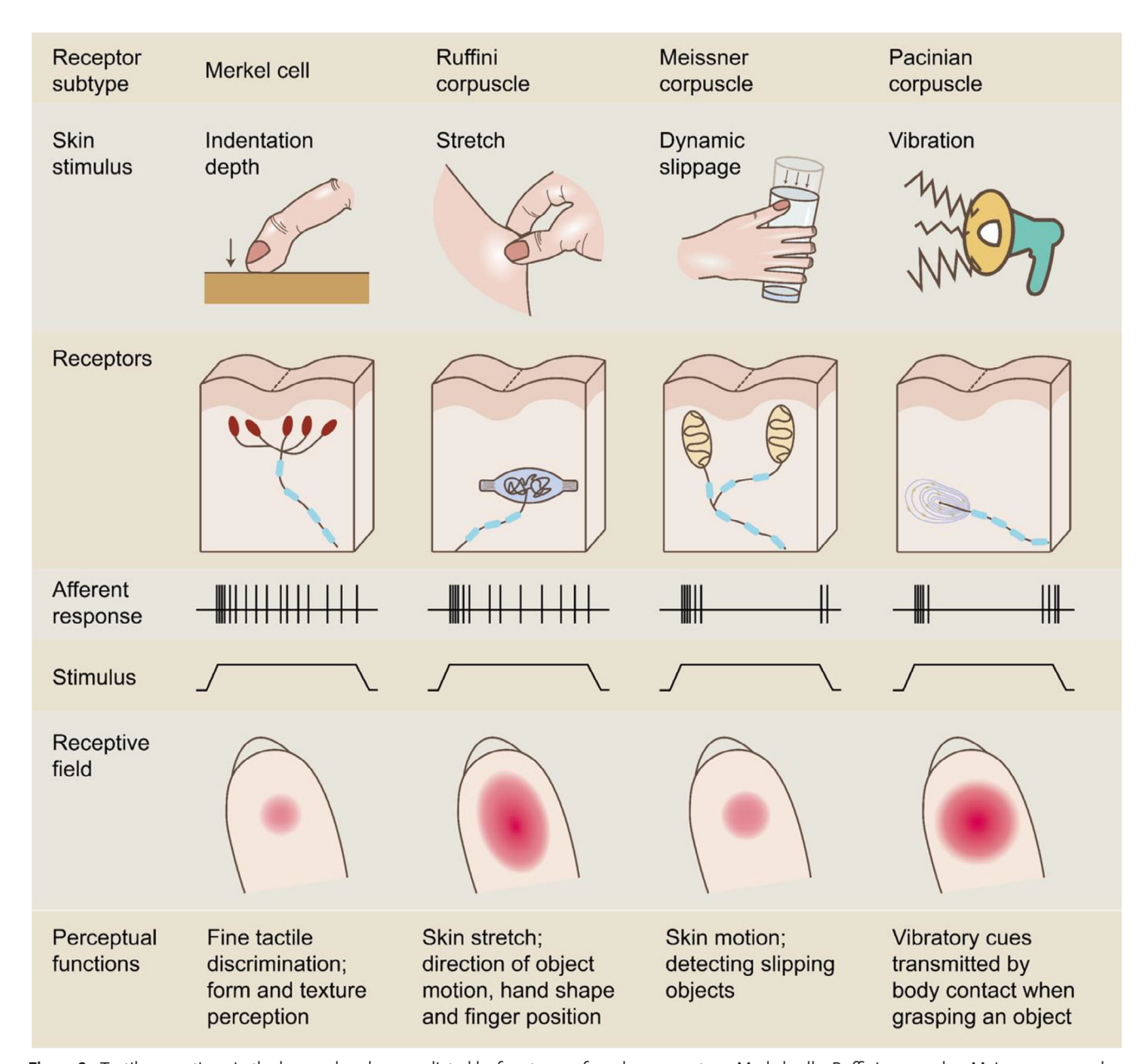


Figure 3. Tactile sensations in the human hand are mediated by four types of mechanoreceptors: Merkel cells, Ruffini corpuscles, Meissner corpuscles, and Pacinian corpuscles. These mechanoreceptors vary in morphology, location within the skin, innervation pattern, receptive field size, physiological responses to touch, and perceptual functions. Adapted with permission.^[55] Copyright 2011, Springer Nature.

shape, color, brightness, distance, and motion of objects.^[76-78] Research in neuroscience and cognitive psychology shows that the brain obtains more than 80% of its information about the surrounding environment through the eyes.^[79,80] The visual information carried by external light is first converted into neuroelectric signals in the human retina. The retina has a layered structure that allows it to perceive and preprocess visual information simultaneously. The extracted information is transmitted through the optic nerve and finally integrated and analyzed in the visual cortex, including pattern recognition and classification, target tracking, and interpretation.^[81]

During a typical day–night cycle, the light intensity at the earth's surface spans an enormous range of 280 dB. [82–84] Although individual retinal neurons are limited to a dynamic range of \approx 40 dB due to their membrane potential constraints, visual adaptation functions enable us to encode and identify objects across vastly different lighting conditions, from starry nights to bright sunlight on a tropical beach (over at least 160 dB). [84,85] Specifically, the human retina achieves this broad sensitivity through two neuronal subsystems that rely on the functioning of two distinct types of photoreceptors: rods and cones (**Figure 4a**). [79,80] Rods are responsible for dark vision, which are highly sensitive to weak light and can be triggered by a single



15214095, 0, Downloaded from https://advanced.onlinelibrary.wiley.com/doi/10.1002/adma.202505420 by HONG KONG POL YTECHNIC UNIVERSITY HU NG HOM, Wiley Online Library on [2609/2025]. See the Terms

and-conditions) on Wiley Online Library for rules of use; OA articles are governed by the applicable Creative Commons!

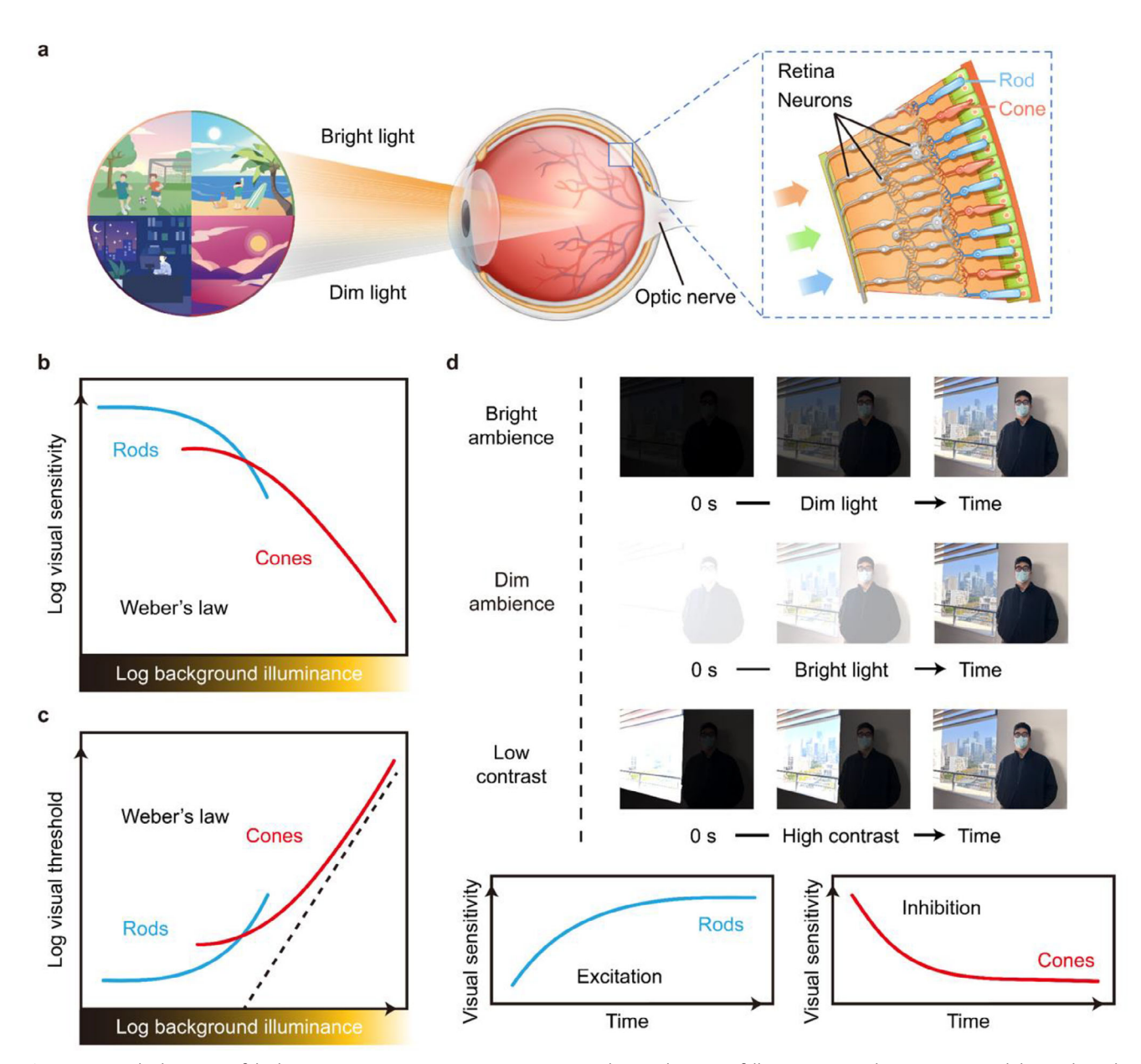


Figure 4. Visual adaptation of the human retina: a) Human vision operates under a wide range of illumination conditions in a normal day-night cycle. The human retina covers this entire range of light intensities with two neuronal subsystems that depend on the activity of two types of photoreceptors: rods and cones. b) The inverse proportionality relationship between sensitivity and light intensity is known as Weber's law. c) Weber's law can also be described as a proportional relationship between visual threshold and background light intensity. The visual threshold is the minimum stimuli intensity required for a person to detect a stimulus. d) Visual adaptation of the human retina. Top: schematic of the time course of scotopic, photopic, and contrast adaptation by images under different ambient lighting conditions. Bottom: light-intensity-dependent antagonistic photoresponses (excitation and inhibition) that rely on two types of neuronal subsystems (rods and cones) are the key mechanisms involved in visual adaptation. a-d) Adapted under the terms of the CC-BY Creative Commons Attribution 4.0 International license (https://creativecommons.org/licenses/by/4.0).[94] Copyright 2024, The Authors, published by Wiley-VCH.

quantum of light. Cones are responsible for daylight vision, providing color recognition and keen vision under bright lights.^[86] The mechanism of human visual adaptation depends on the capacity of the photoreceptors to dynamically regulate their sensitivity to varying ambient light levels. [68,87] According to Weber's law, photosensitivity (S) is inversely related to light intensity (L) (Figure 4b). [88] Mathematically, it can be described as $S/S_0 =$

 $L_0/(L_0 + L)$, where S_0 is the sensitivity in darkness, and L_0 represents the light intensity required to halve the sensitivity.[89] When the background light intensity significantly exceeds L_0 (i.e., for L $\gg L_0$), S is nearly equal to $(S_0 \times L_0)/L$. Given that S_0 and L_0 are both constants, sensitivity decreases in inverse proportion to light intensity, consistent with Weber's law. Furthermore, Weber's law can also be interpreted as the direct proportionality between the



ADVANCED MATERIALS

www.advmat.de

visual threshold and background light intensity (Figure 4c). ^[68] The visual threshold is the minimum stimulus intensity required to detect a stimulus. Mathematically, it can be expressed as $\Delta L = k \times L$, where ΔL is the just perceived change in stimuli, that is, the visual threshold, L is the background stimulus, and k is a constant. When background illumination diminishes (intensifies), the sensitivity of the retina to stimuli increases (decreases), leading to a reduction (elevation) in the visual threshold.

Visual adaptation includes scotopic, photopic, and contrast adaptation (Figure 4d). Scotopic and photopic adaptations represent the adaptability of the retina to the average light intensity. Following the switch from a well-lit environment to a darker one, our eyes can hardly see anything at first and can gradually discriminate the object after scotopic adaptation because retinal sensitivity gradually increases with time. In contrast, following the switch from a dimly lit setting to a brighter one, our eyes are initially dazzled by bright objects and can gradually discriminate them after photopic adaptation, because retinal sensitivity gradually declines with time. Contrast adaptation incorporates both excitatory and inhibitory photoresponses. When exposed from a low-contrast scene to a high-contrast scene, the human retina has the inherent ability to adjust its response to varying light intensities via information preprocessing, which can achieve the amplification required to capture, for example, objects in shadows, while preventing overexposure to bright regions. This dynamic adjustment enables the visual system to perceive subtle details in high-contrast scenarios with higher fidelity compared with a standard camera with a single-exposure setting.[34]

2.3. Auditory, Olfactory, and Gustatory Adaptation

Auditory adaptation is a phenomenon wherein hair cells in the cochlea of the inner ear gradually reduce their responsiveness when exposed to continuous or repetitive sound stimuli. For instance, individuals become increasingly desensitized to background noise after spending time in a loud setting. At the cellular level, extended exposure to sound waves induces a transient inactivation of calcium channels in the hair cell membrane, diminishing neurotransmitter release and lowering the rate of action potential generation. This mechanism not only protects against overstimulation, preventing potential hair cell damage or auditory fatigue but also helps organisms to focus on biologically critical sounds, such as predator noises, or social communication amid complex auditory surroundings. [90,91]

Olfactory adaptation refers to the phenomenon where an organism's olfactory receptors gradually decrease in sensitivity to a particular odor stimulus during prolonged exposure, eventually leading to a temporary inability to perceive the odor. For instance, when entering a coffee shop, one may initially detect a strong coffee aroma; however, this perception diminishes after a few minutes. Similarly, after applying a perfume, individuals may quickly cease to notice the scent themselves, whereas others may still detect it. Mechanistically, odor molecules bind to receptors on olfactory sensory neurons, triggering intracellular signal transduction. However, sustained stimulation induces receptor desensitization or ion channel closure, thereby attenuating signal transmission. This adaptation enables organisms to disregard

constant or irrelevant environmental odors, preventing olfactory overload while enhancing the detection of novel stimuli (e.g., hazards or food sources). [92]

Taste adaptation is the gradual decline in the sensitivity of taste bud receptors upon exposure to prolonged or repeated taste stimulation. For example, although a sugary drink may initially taste very sweet, its perceived sweetness weakens after a few minutes. This occurs because sustained stimulation causes the ion channels on the taste cell membranes to close, thereby lowering the receptor potential. By reducing the sensitivity to persistent flavors, taste adaptation promotes varied eating habits and prevents the overconsumption of specific nutrients.^[93]

Overall, the mechanism of sensory adaptation relies on the gating dynamics of ion channels on receptor membranes and transmembrane transport of relevant ions. For tactile adaptation, the activation and inactivation of ion channels under constant stimulation serve as the primary mechanisms underlying the attenuation (adaptation) of receptor potentials.^[55,60] In visual adaptation, channel-mediated regeneration and bleaching of photopigments constitute fundamental mechanisms that generate both excitatory and inhibitory photocurrents.^[86] These biological principles of sensory adaptation provide crucial insights for designing artificial adaptive sensors.

3. Bioinspired Adaptive Sensors

Biological sensory neurons adapt dynamically to the surrounding environment. This ability provides an efficient neural encoding strategy that enables sensory cells to simultaneously detect, integrate, and preprocess environmental signals.^[26] Recreating the behavior of sensory adaptation using electronic devices has garnered significant research interest owing to its promising applications in next-generation intelligent perception systems. Historically, the hardware implementation of artificial adaptive sensors has typically required dozens of transistors and capacitors interconnected by complex circuits, resulting in high energy consumption and a large footprint.[39-41] In recent years, several emerging devices that naturally exhibit rich neural behaviors have been successfully utilized to replicate sensory adaptation processes, including piezoelectric and triboelectric sensors, [42-45] memristors, [46-48] and neuromorphic transistors.^[49-53] By mimicking biological sensory adaptation mechanisms, such as ion channel activation/inactivation and photopigment bleaching/regeneration,[55,60,86] these devices can realize environmentally adaptable characteristics with a relatively compact structure, simple operational mode, and high energy efficiency.

Herein, we summarize the recent progress in bioinspired adaptive sensors based on these emerging nanoelectronic devices. Notably, distinct from piezoelectric and triboelectric sensors, the development of artificial adaptive sensors based on memristors and neuromorphic transistors mainly follows two approaches. Optoelectronic memristors and phototransistors inherently combine light-sensing and adaptive capabilities within a single device, enabling the emulation of visual adaptation. [94,95] Conversely, electrically driven memristors and neuromorphic transistors generally function as adaptive processing modules, necessitating their additional integration with conventional sensing elements. [96,97]



ADVANCED MATERIALS

www.advmat.de

3.1. Bioinspired Adaptive Piezoelectric and Triboelectric Sensors

Humans perceive tactile sensations through a combination of pressure and vibration information using various types of cutaneous mechanoreceptors.^[98,99] To emulate the functionalities of human skin, artificial tactile sensors based on resistive, capacitive, piezoelectric, and triboelectric mechanisms have been developed to convert mechanical stimuli into electrical signals.[100] Compared with conventional resistive and capacitive sensors with fixed responsivities, piezoelectric and triboelectric sensors exhibit selective sensitivity to dynamic mechanical stimuli. Piezoelectric and triboelectric sensors generate voltage when subjected to mechanical deformation. This deformation alters the magnitude of the dipoles within the active layer, leading to charge accumulation at the electrodes. In piezoelectric materials, dipoles arise from molecular-scale interactions, whereas in triboelectric devices, macroscopic dipoles are generated by contact electrification. Under constant stimulation, the charges that accumulate on the electrodes decay rapidly because of leakage through the external circuit, rendering them ideal for imitating fast-adapting mechanoreceptors.[101] In addition, their ability to generate energy while perceiving mechanical forces enables them to operate efficiently in a self-powered mode. Herein, we discuss the operating principles of piezoelectric and triboelectric sensors, structural design strategies to improve device performance, and their integration with various functional components, including slow-adapting sensors and temperature sensors.

3.1.1. Bioinspired Adaptive Piezoelectric Sensors

A piezoelectric tactile sensor generates an instantaneous piezoelectric potential when stretched or compressed by a mechanical force. [101] The sensor is typically structured as a piezoelectric material enclosed between two parallel electrodes. The key characteristics of piezoelectric materials are their noncentrosymmetric crystal structures and inherent electric dipole moments. [102] The application of mechanical stress to a piezoelectric material can change the density of polarized dipoles, thus producing an instantaneous voltage output. Based on the relationship between the stress/strain direction and the polar-axis direction in the material, a piezoelectric tactile sensor can primarily have two working modes: the d_{33} and d_{31} modes (Figure 5a). [103] If the direction of the applied mechanical stress is parallel to the polar-axis direction, the sensor operates in the d_{33} mode; if this direction is perpendicular, it operates in the d_{31} mode. In recent years, a wide range of piezoelectric materials has been explored for dynamic force detection, encompassing inorganic piezoelectric materials such as zinc oxide (ZnO) and barium titanate (BaTiO₃); organic piezoelectric materials, such as poly(vinylidene fluoride) (PVDF) and poly(vinylidene fluoride trifluoroethylene) (P(VDF-TrFE)); and composite piezoelectric materials. [102,103] Some structural design strategies have also been implemented to enhance the performance of piezoelectric sensors.[100-103]

Inspired by the human limb structure in which the skeleton is integrated into the muscle, Zhang et al. designed a hybrid rigid-soft piezoelectric haptic sensor with exceptional sensitivity for dynamic stimuli detection.^[104] As illustrated in Figure 5b, the sensor comprises three layers, including a hybrid rigid-soft force

transmission layer, a PVDF-based piezoelectric sensing layer, and a soft bottom substrate. The bioinspired hybrid rigid-soft structure not only efficiently transfers high-frequency dynamic force to the piezoelectric sensing layer but also triggers a remarkable amplification effect in a new d_{31} mode with the assistance of the soft bottom substrate (Figure 5c). Experimental results have shown that the tactile sensor reaches a peak sensitivity of 346.5 pC N⁻¹ at 30 Hz, surpassing the theoretical limit of the conventional d_{33} mode (21 pC N⁻¹) by a factor of \approx 17 (Figure 5d,e). Owing to its exceptional sensitivity to vibrational stimuli, the piezoelectric tactile sensor array was mounted on a robotic hand to record the entire dynamic process of water pouring. This includes actions such as grasping of a bottle, holding it, receiving water (vibrational stimulus), sliding, and placing the bottle down. To enhance the piezoelectric properties of PVDF thin films, Wang et al. prepared PVDF nanorod arrays via hot pressing using an anodic aluminum oxide template. [105] When subjected to the same ultrasonic power, the amount of charge generated by a PVDF nanorod array was found to be more than 10 times that generated by an ordinary PVDF film. In addition, drawing inspiration from the multilayer structure of the human skin, Lin et al. developed a piezoelectric haptic sensor array that included two PDMSbased protective layers, two PVDF-based sensing layers, and one PDMS-based insulation layer.[106] The unique multilayer design combined with row + column electrodes can effectively eliminate crosstalk issues and significantly decrease the number of connection wires when manufacturing piezoelectric sensor arrays with a larger area and high resolution. In particular, only n + m wires are required for an n x m sensing array. Notably, sensory adaptation enhances the sensitivity to future stimulus variations by diminishing the signal output under constant stimulation. For instance, under a fixed pressure of 10 kPa, when a new stimulus of 20 kPa was applied, the adaptive device exhibited a significantly higher sensitivity (5 kPa⁻¹) than conventional pressure sensors (0.08 kPa⁻¹).[97]

In addition to improving the performance of piezoelectric haptic sensors, their integration with other functional elements, such as slow-adaptive sensors and temperature sensors, can help completely mimic human skin sensations and provide enhanced functionalities beyond a single piezoelectric sensor. Qiu et al. engineered a bimodal haptic sensor comprising a P(VDF-TrFE)based piezoelectric layer and a piezoresistive layer composed of carbon nanotubes and silicone rubber composites (Figure 5f).[107] When an external mechanical force is transferred from the top bump-shaped layer to the sensory layer, the piezoelectric layer generates an instantaneous response, mimicking rapidly adapting mechanoreceptors, while the piezoresistive layer produces a sustained response, similar to slow-adapting mechanoreceptors (Figure 5g,h). Similarly, Chun et al. designed a self-powered bimodal haptic sensor by spatially integrating an artificial ion channel system and a piezoelectric film.[108] The tactile sensor comprises an Al/C bottom electrode, a polyaniline (PANI) electrolyte, a pore membrane (MB), and a PVDF piezoelectric film sandwiched between two Au electrodes. When pressure is applied to the sensor, the PVDF layer generates a piezoelectric potential to simulate fast-adaptation signals, whereas ion movement through the pore membrane in the PANI electrolyte exhibits the characteristics of slow-adapting mechanoreceptors. Zhu et al. demonstrated a vertically configured



15214095, 0, Downloaded from https://advanced.onlinelibrary.wiley.com/doi/10.1002/adma.202505420 by HONG KONG POLYTECHNIC UNIVERSITY HU NG HOM, Wiley Online Library on [26/09/2025]. See the Terms

and-conditions) on Wiley Online Library for rules of use; OA articles are governed by the applicable Creative Commons I.

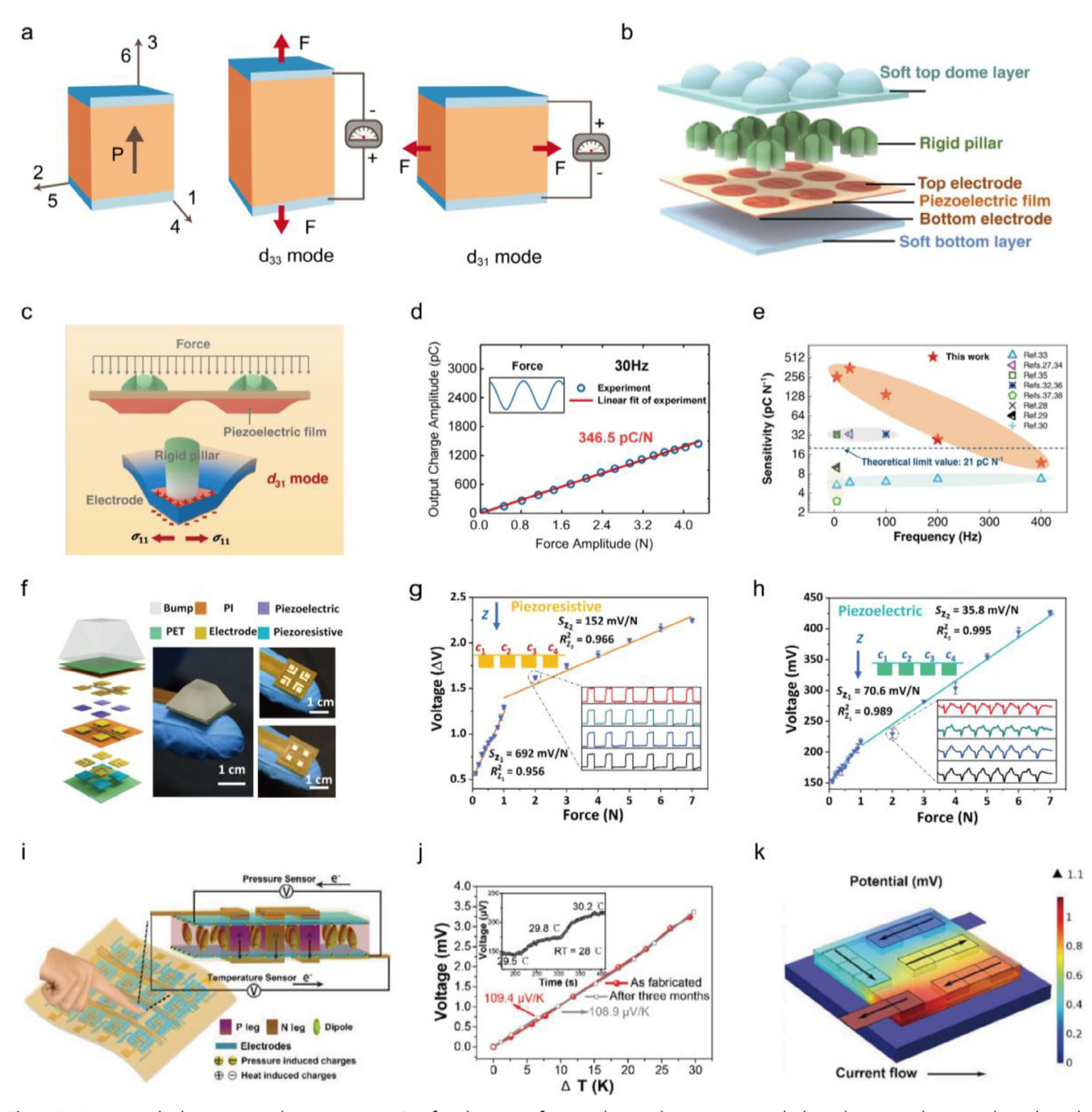


Figure 5. Bioinspired adaptive piezoelectric sensors: a) Left: schematic of a typical piezoelectric sensor with the polarization direction along three directions. Middle: schematic of the d_{33} working mode. Right: schematic of the d_{31} working mode. b) Finger-inspired hybrid rigid—soft piezoelectric tactile sensor array. c) Working mode of the tactile sensor. d) Output charge of the tactile sensor as a function of the applied normal force measured at 30 Hz. e) Comparison of the sensitivity of the tactile sensor with existing piezoelectric tactile sensors. b-e) Reproduced under the terms of the CC-BY Creative Commons Attribution 4.0 International License (http://creativecommons.org/licenses/by/4.0/).[104] Copyright 2022, The Authors, Published by Springer Nature. f) Detailed structure and optical images of a bimodal haptic sensor. g) Voltage response of the bimodal sensor based on piezoresistive mechanism. h) Voltage response of the bimodal sensor based on piezoelectric mechanism. f–h) Reproduced under the terms of the CC-BY Creative Commons Attribution 4.0 International License (http://creativecommons.org/licenses/by/4.0/). [107] Copyright 2024, The Authors, Published by American Association for the Advancement of Science. i) Schematic of the working principle of vertically stacked bimodal sensor. j) Voltage response of the device showing high-temperature detection sensitivity. k) Potential profiles of the sensor simulated by a 3D finite element analysis. i–k) Reproduced with permission.[109] Copyright 2020, Wiley-VCH.



ADVANCED MATERIALS

www.advmat.de

flexible piezothermoelectric-integrated bimodal sensor array. [109] The device was fabricated using a piezoelectric P(VDF-TrFE)based film and a thermoelectric PANI-based composite. Figure 5i illustrates the working principles of the two vertically stacked sensing units. This clearly shows that the bimodal sensor enables synchronous piezoelectric and thermoelectric conversion with independent signal transmission circuits for each modality. Meanwhile, the sensor shows high-temperature detection sensitivity (109.4 μV K⁻¹) and a wide pressure sensing range (100 Pa to 20 kPa) (Figure 5j). Using a 3D finite element analysis, the authors further simulated the potential distribution within the sensor induced by ambient temperature stimuli (Figure 5k). The resulting potential distribution was in good agreement with the experimentally measured temperature-dependent electrical characteristics. In another study, Park et al. developed a multimodal electronic skin based on a microstructured ferroelectric composite film composed of PVDF and reduced graphene oxide (rGO) to distinguish between static and dynamic pressures, as well as temperature stimuli.[110] Specifically, the dynamic pressure and temperature variations were monitored through the piezoelectric and pyroelectric characteristics inherent in ferroelectric composites, whereas the change in the contact resistance between interlocked microdome arrays was used to detect the static pressure.

3.1.2. Bioinspired Adaptive Triboelectric Sensors

With the coupling of the principles of contact electrification and electrostatic induction, a triboelectric tactile sensor can generate instantaneous electrical signals when subjected to mechanical stimuli.[111] A triboelectric tactile sensor typically contains at least two components: a dielectric material and a conductive electrode. Depending on device configuration and operation styles, triboelectric tactile sensors operate in four fundamental modes: vertical contact separation, single electrode, lateral sliding, and freestanding triboelectric layer.[112] Among them, the contactseparation mode is the most commonly used, and it includes two dielectric materials with different electronegativities and two conductive electrodes (Figure 6a). During the contact-separation process, the dielectric layer generates triboelectric charges, and the electrode layer collects the generated charges. Owing to their simple device structure, wide range of material availability, flexibility, ease of fabrication, and scalability, triboelectric devices have emerged as core components of self-powered sensors/systems for dynamic stimulus detection.[113,114]

Similar to piezoelectric tactile sensors, various structural design strategies have been explored to enhance the performance of triboelectric tactile sensors. For instance, Huang et al. fabricated multiscale architectures on both the triboelectric layers using the femtosecond laser direct writing method. As shown in Figure 6b, the fabricated micro/nanostructures contain micro/nanocones on the Cu surface and microbowl structures on the PDMS surface. With the developed micro/nanostructures, the effective contact area and surface roughness could be significantly increased, and the power density was enhanced by $\approx\!21$ times compared with that without micro/nanostructures. Furthermore, Yu et al. designed a piezoelectric-enhanced triboelectric sensor with high sensitivity (18.96 V kPa $^{-1}$ and 0.18 μ A kPa $^{-1}$ across a broad pressure range of 100–800 kPa) and a wide de-

tection range (0-1300 kPa).[116] Specifically, the polarized microfrustum array of lead zirconate titanate (PZT) and PDMS composite film (m-PZT&PDMS) generates piezoelectric signals during deformation, whereas the interaction between nonpolarized m-PZT&PDMS and the micro-frustum array of the Cu film contributes to the generation of triboelectric signals through the contact-separation mode. Owing to its high sensitivity to dynamic stimuli, the tactile sensor can be attached to the heel as a gait monitor, enabling the comprehensive tracking of human motion postures. By statistically analyzing the waveform characteristics, amplitude, and frequency of the generated triboelectric signals, it can accurately distinguish a series of activities such as walking, brisk walking, running, tiptoeing, and jumping. Qu et al. developed a triboelectric tactile, intelligent sensing finger that operates in the single-electrode mode (Figure 6c).[117] To effectively identify external stimuli, the triboelectric sensor array contains four separate sensors in each sensing unit. Four different triboelectric materials-polyamide (PA66), polyethylene terephthalate (PET), polystyrene (PS), and polytetrafluoroethylene (PTFE) were utilized as friction layers. When the tactile perception array is in contact with the test material, each sensor generates a unique output signal with varying amplitudes and waveforms, owing to the different capabilities of the material to gain or lose electrons (Figure 6d,e). This combination of sensors significantly enriches the characteristic information of the measured materials. With the assistance of machine learning, the material identification rate can reach an impressive 96.8%.

To emulate the multisensory capability of the human skin, Wu et al. reported a single-mode and self-powered tactile sensor exhibiting both fast and slow adaptation by combining triboelectric and potentiometric sensing principles.[118] As illustrated in Figure 6f, the device structurally integrates two functional components: a triboelectric module and a potentiometric module. The triboelectric module comprises a microstructured PDMS friction layer and an Al electrode layer. The potentiometric module comprises a microstructured electrolyte (poly(vinyl alcohol)/sodium chloride/glycerol (PVA/NaCl/Gly) ionic composite), a sensing electrode (Prussian blue-modified graphite carbon), and a reference electrode (Ag/AgCl). When the mechanical stimulus is transmitted from the top triboelectric layer to the bottom potentiometric layer, a single-mode voltage signal is generated, including two triboelectric spikes with a potentiometric plateau sandwiched between them (Figure 6g). This single-mode signal output enables streamlined device operation and minimizes the complexity of the measurement circuit. Wang et al. developed a multilayer stacked multifunctional sensor by combining triboelectric, piezoresistive, and thermoelectric effects. [119] The sensor was mainly composed of a hydrophobic PTFE film, a sponge-like graphene/PDMS composite film, and two Cu sheets coated with a silver nanowire film. Figure 6h,i shows the simulated strain distribution and electric potential of the graphene/PDMS composite under mechanical pressure and thermal gradients, respectively. This indicates that the graphene/PDMS sponge could simultaneously detect pressure and temperature variations via coupled piezoresistive and thermoelectric transduction mechanisms. Moreover, when the PTFE film contacts an object, it generates a triboelectric potential induced by Maxwell's displacement currents, enabling material identification (Figure 6j).

15214095, 0, Downloaded from https://advanced.onlinelibrary

wiley.com/doi/10.1002/adma.202505420 by HONG KONG POLYTECHNIC UNIVERSITY HU NG HOM, Wiley Online Library on [26/09/2025]. See the Terms

nditions) on Wiley Online Library for rules of use; OA articles are governed by the applicable Creative Common

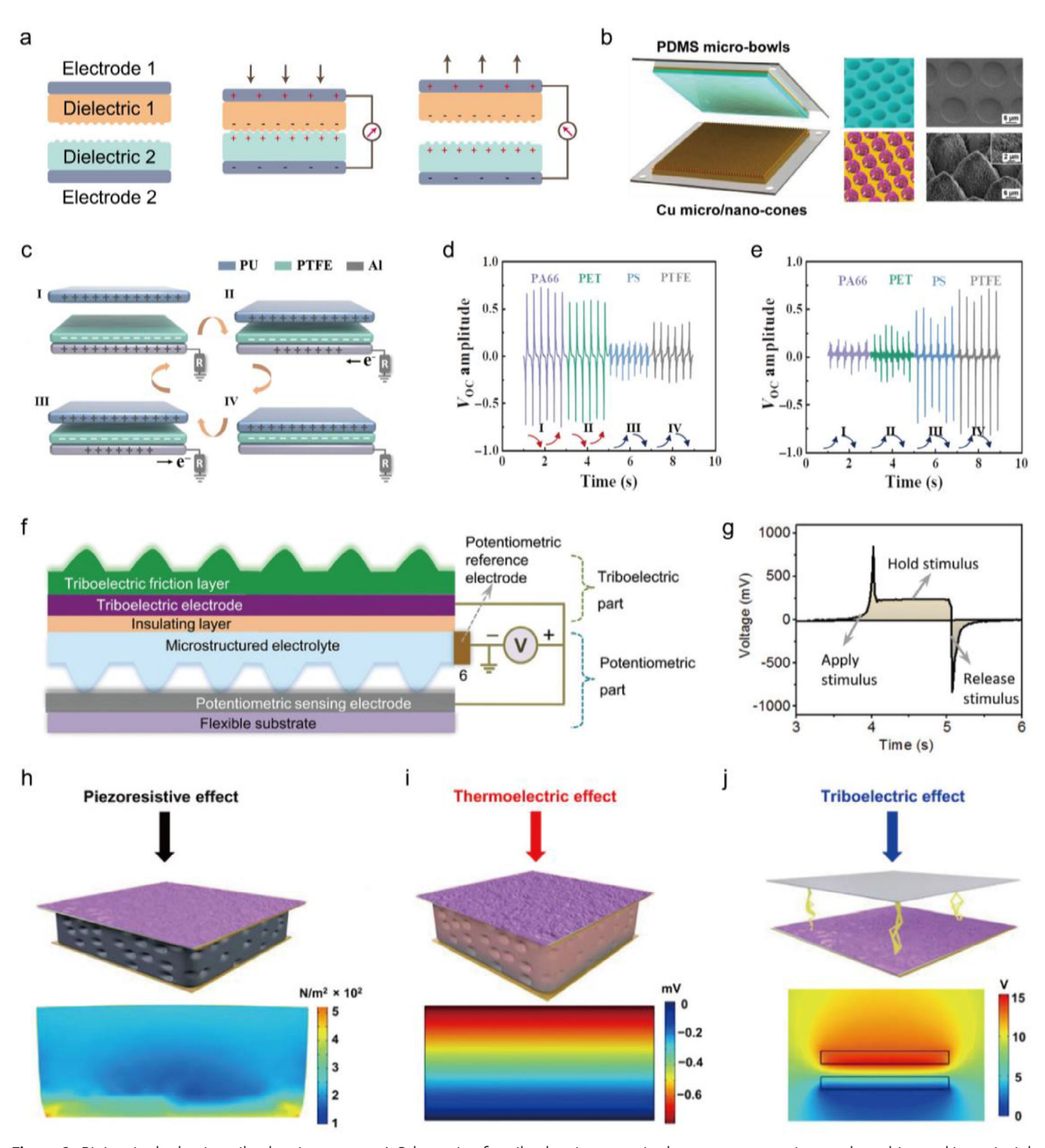


Figure 6. Bioinspired adaptive triboelectric sensors: a) Schematic of a triboelectric sensor in the contact-separation mode and its working principle. b) Fabricated micro/nano structures include a micro/nano-cone structure on Cu surface and a micro-bowl structure on PDMS surface; Reproduced with permission. Copyright 2019, Elsevier. c) Working mechanism of triboelectric sensing based on single electrode mode. d) V_{oc} amplitude output of each triboelectric sensor when the sensor array identifies PS. e) V_{oc} amplitude output of each triboelectric sensor when the sensor array identifies PA66; c–e) Reproduced with permission. Copyright 2022, American Association for the Advancement of Science. f) Schematic depicting the configuration design of the mechanoreceptor. g) Signal output of the mechanoreceptor operating in the hybridized mode. f,g) Reproduced with permission. Copyright 2020, Wiley-VCH. h) Simulated strain field of the graphene/PDMS composite under mechanical pressure. i) Simulated electric potential of the graphene/PDMS composite under temperature gradient. j) Electric potential on the PTFE when it is in contact with the object. h–j) Reproduced under the terms of the CC-BY Creative Commons Attribution 4.0 International License (http://creativecommons.org/licenses/by/4.0/). Copyright 2020, The Authors, Published by American Association for the Advancement of Science.

b a Ag electrode FLBP-CsPbBr, PDMS substrate Self-assemble CsPbBr. FLBP NSs QDs FLBP-CsPbBr. d е Adaptive neuromorphic sensory system Light perceptual mode Voltage Stimulus Input Current (µA) $I_B = 100 \,\mu\text{W/cm}^2$ Sensing device Memristor 0 Substrate Light Sensor Pressure Sensor Temperature Senso (3) 0.22 mW/cm

Figure 7. Adaptive memristive synaptic devices: a) Schematic of the switching mechanism of the ionic memristor. b) Schematic of the threshold switching memristor with the structure of Ag/few-layer black phosphorous nanosheets–CsPbBr₃ perovskite quantum dots (QDs) heterostructure (FLBP-CsPbBr₃)/indium tin oxide (ITO); Reproduced under the terms of the CC-BY Creative Commons Attribution 4.0 International License (http://creativecommons.org/licenses/by/4.0/). Copyright 2021, The Authors, Published by Springer Nature. c) Schematic of the complementary memristor. d) Schematic of the adaptive neuromorphic sensory system with multiple perceptual modes. e) Adaptive response to light stimulation. c–e) Reproduced with permission. Self-active Complementary of a planar optoelectronic memristor based on multilayer γ-InSe flakes. g) Normalized real-time I_{DS} of the device under bright light irradiation (power density: 60 mW cm⁻²) with wavelength between 300 and 1000 nm. f,g) Reproduced under the terms of the CC-BY Creative Commons Attribution 4.0 International License (http://creativecommons.org/licenses/by/4.0/). Copyright 2023, The Authors, Published by Springer Nature. h) Excitation and inhibition of the photocurrent response of the Au/ZnS/Pt memristor; Reproduced under the terms of the CC-BY Creative Commons Attribution 4.0 International license (https://creativecommons.org/licenses/by/4.0). Copyright 2022, The Authors, published by Wiley-VCH.

3.2. Bioinspired Adaptive Memristors

Neuromorphic computing, which draws inspiration from the information-processing rules of the biological nervous system, is a disruptive computing technology for sophisticated cognitive tasks with robust processing power and high energy efficiency. [120–125] Memristors have emerged as leading contenders for neuromorphic computing owing to their simple two-terminal structure, ultrahigh-density 3D integration, low energy consumption, high switching speeds, and in-memory processing capacity. [126–129] Owing to their unique stimulus-history-dependent response characteristics, memristors have been widely developed to replicate the operational dynamics of

biological synapses and neurons.^[130-132] Specifically, memristors are devices that can exhibit two or more resistance states upon a sequential application of voltage or current signals.^[133,134] The resistance switching mechanism can be attributed to ion migration, electron trapping, phase transition, spin polarization, and ferroelectric polarization.^[135,136] In particular, for ionic memristors, the formation and breakdown of nanoscale conductive filaments induced by ion transport are analogous to the activation and deactivation dynamics of ion channels in the receptor membrane (**Figure 7a**).^[137,138] Such a similarity makes ionic memristors ideal devices for constructing artificial adaptive sensors with high fidelity and dynamic modulation functions.^[139,140]



ADVANCED MATERIALS

www.advmat.de

3.2.1. Adaptive Memristive Synaptic Devices

In addition to integrating storage and processing capabilities. memristive synaptic devices can adjust the information transmission efficiency, which can be used to simulate the sensory adaptation functionality of biological receptors.[141-143] For example, Liu et al. reported an adaptive synaptic device based on a TiN/Li_SiO_/Pt memristor.[144] Under a consecutive identical pulse (voltage of 3.4 V, duration of 10 µs, interval of 10 µs), the current response of a Li_vSiO_v-based memristor undergoes a rapid surge at the onset of stimulation, followed by a gradual decline during the remaining stimulation period, exhibiting functional resemblance to biological sensory adaptation. The results of highresolution transmission electron microscopy helped confirm that this adaptive behavior originates from the formation and rupture of crystalline lithium titanium silicate (LiTiSiO₄) channels. A similar non-monotonic conductance response was implemented by Wang et al. using a light-mediated threshold switching memristor, which comprised a structure of Ag/few-layer black phosphorous nanosheets-CsPbBr3 perovskite quantum dot (QDs) heterostructure (FLBP-CsPbBr₃)/ITO (Figure 7b).^[145] When a programming electronic pulse (voltage of 0.2 V, duration of 50 us, interpulse interval of 50 us) and an optical stimulus (wavelength of 365 nm, power of 2.5 mW) were applied simultaneously, the conductance of the FLBP-CsPbBr3 threshold switching memristor increased, reached a peak value, and then decreased. In this case, the applied light stimulation could regulate the formation and rupture of the Ag conductive filaments. Song et al. developed an adaptive diffusion memristor using a stack of Pt/Ag/SiO₂ nanorods/Ag/Pt.^[146] Owing to their unique porous nanorod structure, the diameter of the filaments formed by the electromigration of the active metal Ag can be effectively controlled using the amount of Ag. For thin Ag conductive filaments, Joule heat induces filament rupture, leading to adaptation. In another study, Shi et al. developed a Ag nanowire-embedded sodium alginate-based complementary memristor, where the temporal response under continuous voltage stimuli was analogous to that of sensory adaptation (Figure 7c). [96] By combining complementary memristors with commercial light, pressure, and temperature sensors, three types of neuromorphic sensory systems were constructed to realize adaptive visual, tactile, and temperature perceptions (Figure 7d,e). This study demonstrated the general applicability of memristors as adaptive processing units in the development of various adaptive sensing systems.

Unlike electrically stimulated memristive devices, optoelectronic memristors can integrate light-detection and adaptation capabilities into a unified device. [147,148] Recently, various photoactive materials and operating principles have been investigated to develop optoelectronic memristors that can autonomously adapt to different lighting conditions. For instance, Chen et al. engineered an adaptive photovoltaic memristor using a triple-cation mixed-halide Cs_{0.05}FA_{0.81}MA_{0.14}PbI_{2.55}Br_{0.45} (CsFAMA) perovskite. [149] Owing to the ion migration-driven photovoltaic switching behavior, the photoresponsivity of the Au/CsFAMA/ITO memristor can be reconfigured over a wide range. Specifically, the maximum photocurrent relaxation can reach 540% under a light intensity of 96 mW cm⁻². In addition, Xu's group demonstrated a self-powered 2D γ-InSe-based planar optoelectronic memristor, realizing photopic adaptation

functionality (Figure 7f).[150] As shown in Figure 7g, the device exhibits a broadband optoelectronic adaptation behavior (at wavelengths ranging from 325 to 1550 nm), which is enabled by the narrow bandgap of γ -InSe. This dynamic adaptation can be attributed to the coupled photopyroelectric and photothermoelectric effects. In a dazzling environment, the initial swift decay stage is predominantly driven by the photopyroelectric effect, whereas the ensuing gradual decay stage is largely attributed to the photothermoelectric effect. Geng et al. developed an adaptive photoelectric synaptic memristor with a simple Au/ZnS/Pt structure.[151] The device can operate in both the excitation and inhibition photocurrent modes; therefore, it can emulate scotopic and photopic adaptations (Figure 7h). The inhibited photocurrent mode originates from the photoexcited carriers trapped by defects in the ZnS thin films. The excitation photocurrent mode is achieved via pre-stressed voltage stimulation, which can induce trap filling.

3.2.2. Adaptive Memristive Spiking Neurons

Biological neurons encode sensory information by firing neural spikes, which are characterized by distinct temporal patterns. An adaptive encoding pattern is characterized by a reduced spike frequency over time. Typically, there are two primary strategies for achieving this adaptive spiking characteristic using memristors. One strategy is based on a single threshold-switching memristor, which takes advantage of the inherent physical attributes of the device. For instance, Xie et al. demonstrated an ionic memristor based on Pt/Co₃O_{4-x}/ITO that could realistically generate adaptive voltage spike trains through its internal ion dynamics (Figure 8a-c).[152] Specifically, this adaptive spike behavior is attributed to the dynamic interconversion between Joule-heatdriven filament breakage and electric-field-assisted filament reconstruction under bias current modulation. An artificial tactile neural system was constructed through a seamless integration of the adaptive memristor with a pressure sensor (Figure 8d). The system could sensitively perceive subtle pressure signal changes and recognize dynamically stacked objects with a high accuracy of 95.3%. Zhuge et al. reported a novel bimode memristive neuron that can respond to excitatory and inhibitory inputs.[153] As shown in Figure 8e, the device comprises a bipolar threshold-switching memristor based on Cu/ZnS/Pt. Owing to its unique bipolar threshold-switching behavior, the threshold voltage of the memristor can be reversibly adjusted using positive and negative voltages. Similarly, this bimode memristive neuron can be used to simulate light and dark adaptation functionalities.

Alternatively, adaptive memristive spiking neurons can be implemented by integrating adaptive memristive synaptic devices with simple circuits. For example, Liu et al. constructed an adaptive memristive spiking neuron by connecting a $\rm Li_xSiO_y$ -based adaptive memristor to a Ag-based leaky integrate-and-fire neuron. [144] As illustrated in Figure 8f, the neuron circuit comprises a threshold switching memristor (Ag/SiO₂:Ag/Au), a capacitor (100 nF), and a resistor (10 k Ω). When a series of identical stimulation pulses (voltage of 4.0 V, duration of 700 μ s, interval of 300 μ s) is applied to the integrated system, significant adaptive spiking behavior can be observed (Figure 8g). In the

15214095, 0, Downloaded from https://advanced.onlinelibrary.wiley.com/doi/10.1092/adma.202505420 by HONG KONG POLYTECHNIC UNIVERSITY HU NG HOM, Wiley Online Library on [2609)2025]. See the Terms and Conditions (https://onlinelibrary.wiley.

om/terms-and-conditions) on Wiley Online Library for rules of use; OA articles are governed by the applicable Creative Commons I

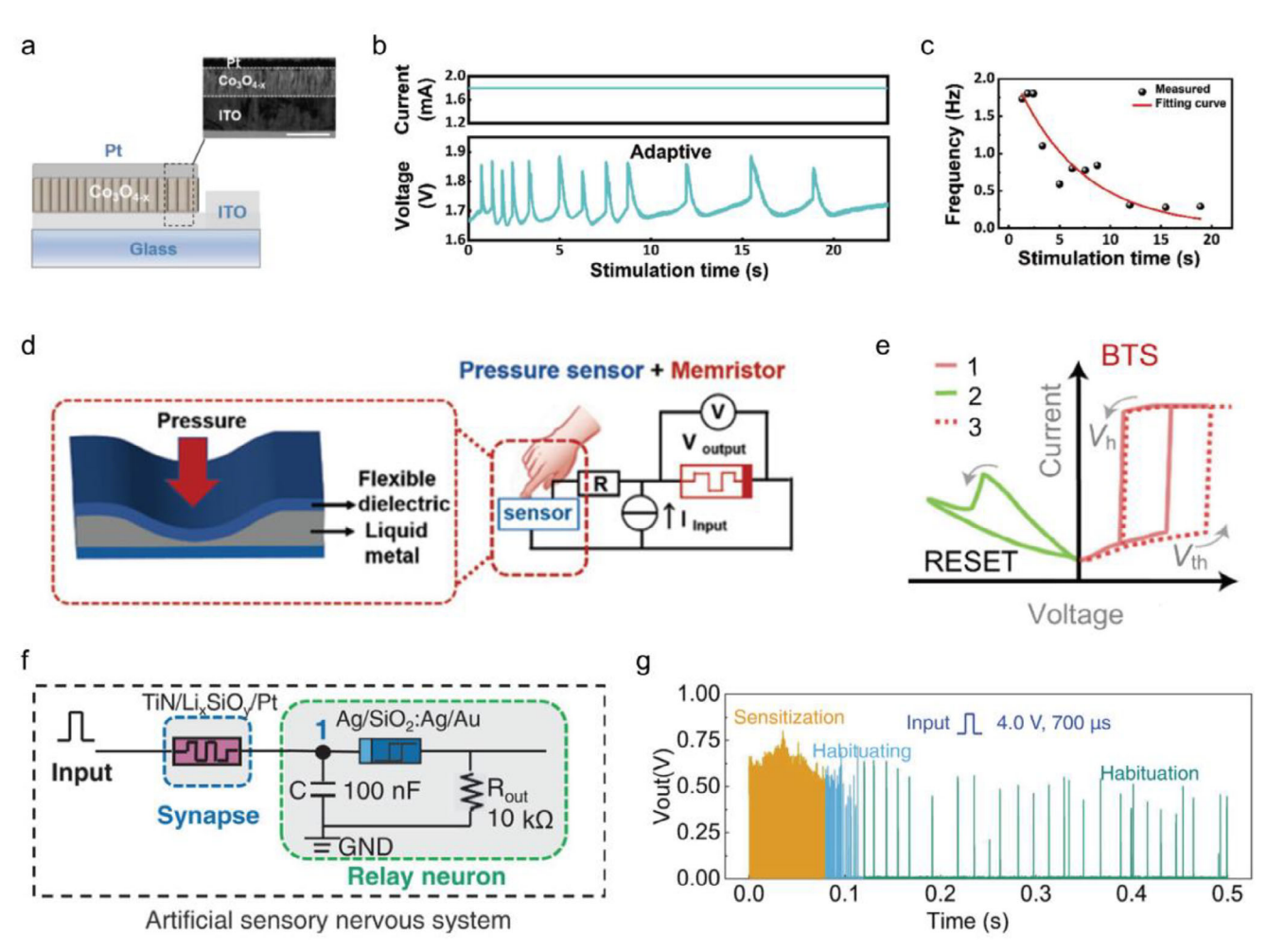


Figure 8. Adaptive memristive spiking neurons: a) Schematic of the Pt/Co₃O_{4-x}/ITO memristor. Inset: Cross-sectional TEM image of the memristor. Scale bar: 200 nm. b) Adaptive firing pattern of the memristor, showing reduced spike frequency over time. c) Spike frequency as a function of the stimulation time. d) Circuit diagram of the memristor-based artificial tactile sensory neuron. a–d) Reproduced with permission. [152] Copyright 2022, Wiley-VCH. e) I-V characteristics of a bipolar threshold switching memristor; Reproduced with permission. [153] Copyright 2024, American Chemical Society. f) Fully memristor-based artificial adaptive spiking neuron circuit, comprising a synaptic device (TiN/Li_xSiO_y/Pt) and a neuron constructed by a threshold switching memristor (Ag/SiO₂:Ag/Au), a capacitor (100 nF), and a resistor (10 kΩ). g) Output spikes of the fully memristor-based artificial adaptive spiking neuron circuit. f,g) Reproduced with permission. [144] Copyright 2020, Wiley-VCH.

time window ranging from 0 to 0.1 s, the adaptive memristive synaptic device operates in a low-resistance state, resulting in an integrated system producing a high-frequency output (≈1 kHz). However, from 0.1 to 0.5 s, the adaptive memristive synaptic device transitions to a high-resistance state, causing the spiking frequency of the integrated system to decrease to ≈80 Hz. Shaban et al. developed a double-exponential adaptive threshold (DEXAT) neuron model with enhanced computational accuracy, accelerated convergence rates, and tunable memory timescales for neuromorphic recurrent spiking neural networks (RSNNs).[154] This DEXAT neuron model can be physically implemented through device-circuit co-optimization in hybrid oxide-based resistive memory (CMOS-OxRAM) platforms. Using the parameters of the DEXAT neurons extracted from experiments, the systemlevel RSNN simulation achieved a test accuracy of 96.1% for the classification of sequential MNIST (SMNIST) handwritten digits.

3.3. Bioinspired Adaptive Neuromorphic Transistors

In a three-terminal neuromorphic transistor, the source, drain, and gate are isolated by a semiconductor and a dielectric layer. [155,156] The application of voltage to the gate terminal induces charge carriers at the dielectric–semiconductor interface, which in turn increases channel conductivity. Typically, charge trapping in a three-terminal transistor leads to attenuation of the channel current, which is not conducive to the stability of the device performance. [157] A controllable current decay is a remarkable feature of artificially adaptive devices. In recent years, fine-tuning of the charge trapping and de-trapping processes through the gate voltage has emerged as an effective strategy to achieve sensory adaptation in three-terminal neuromorphic transistors, particularly visual adaptation. Depending on the location of charge trapping, these artificial adaptive neuromorphic transistors can be divided into two categories: dynamic trapping in





www.advmat.de

the channel layer and dynamic trapping in the dielectric layer (Figure 9a).

3.3.1. Dynamic Trapping in the Channel Layer

Charge trapping in the channel layer can directly cause output current decay in a three-terminal neuromorphic transistor. Jiang et al. reported such an adaptive transistor based on a gatedmodulated 0D-CsPbBr3-QDs/2D-MoS2 mixed-dimensional van der Waals heterostructure.[158] The prepared device exhibited key adaptive characteristics, including adjustable accuracy, controllable sensitivity, desensitization, and inactivation, attributed to the charge trapping/de-trapping processes in the space charge region of the heterojunction. Visual adaptation functionality, enabled by an environmentally adjustable threshold, has also been effectively demonstrated through an optoelectronic synergistic approach. More recently, Jiang et al. reported a neuromorphic transistor utilizing a porous metal-organic framework (UiO-66-NH2)/ReS2 heterojunction, which achieved polarization-perceptual visual adaptation (Figure 9b).[159] Owing to the in-plane structural anisotropy of 2D ReS2 and the dynamic charge trapping/de-trapping mechanisms within the heterojunction interfaces, neuromorphic transistors exhibit inherent polarization sensitivity and unique adaptability. Various polarization-sensitive neuromorphic functions, including the multimode adjustable dichroic ratio, excitatory postsynaptic current (EPSC), and reconfigurable sensory adaptation, were simulated using the heterojunction phototransistor. Crucially, the polarization adaptation strongly depends on the applied gate voltage and external background lighting environment (Figure 9c-e).

Chai et al. developed a bioinspired phototransistor that mimicked the visual scotopic and photopic adaptation functionalities. [95] The phototransistor is fabricated with doublelayer MoS₂ on a high- κ dielectric layer (Figure 9f). To introduce charge trap states on the surface of MoS2, ultraviolet/ozone treatment was directly performed on the MoS2 channel. Depending on the polarity of the applied gate voltage, these defect states can trap or de-trap electrons in the channel and lead to two characteristics: current inhibition or current excitation (Figure 9g). Moreover, the light-intensity-dependent behavior of the phototransistor aligns with Weber's law, demonstrating that the visual threshold is proportional to the background intensity (Figure 9h). Similarly, Zhang et al. demonstrated a near-infrared heterojunction phototransistor capable of adapting to irradiance. [160] A vertically stacked graphene/lead sulfide (PbS) QD/graphene structure was utilized as a conductive channel. The gate-voltage-regulated temporal photoresponse (inhibition and excitation) is achieved by adjustable charge trapping/detrapping processes in the PbS QD film, which contains a high density of electron trap states. Consequently, environmentally adaptable (scotopic and photopic) functionalities can be successfully mimicked. Shi et al. reported a flexible, ion-modulated 28 × 28 phototransistor array with scotopic and photopic adaptations (Figure 9i).[161] The phototransistor comprises a 2D MoS₂/graphdiyne heterostructure and a polymer electrolyte. When gate voltages with different polarities were applied, Li+ ions intercalated and deintercalated in the graphdiyne layer,

thus realizing the two characteristics of inhibition and excitation (Figure 9j).

3.3.2. Dynamic Trapping in the Dielectric Layer

Charge trapping within the dielectric layer can induce a volatile shielding effect on the effective gating field, leading to selfadaptive carrier concentration modulation in the conductive channel. Shen et al. fabricated an organic adaptive transistor by introducing a buried charge-trapping interface (PBTTT/PVA) within the poly(vinyl cinnamate) dielectric architecture, as illustrated in Figure 10a.[97] Figure 10b presents the time-dependent $I_{\rm DS}$ ($V_{\rm DS} = -1$ V) response of the device upon $V_{\rm GS}$ pulse (-4 V). Interestingly, a rapid and repeatable decay of I_{DS} was observed under constant $V_{\rm GS}$ and $V_{\rm DS}$. With such unique behavior, a series of advanced biological functionalities, including dynamic speed recording, sensitivity enhancement, and habituation, can be emulated using an organic adaptive transistor. More importantly, by substituting the electron trapping dielectric layer or changing the thickness of PBTTT, the device could exhibit a fine-tuned decay constant (τ) ranging from 50 ms to 5 s, accurately matching the adaptation timescale of the biological system (Figure 10c). He et al. developed a photo-triggered organic active adaptation transistor that incorporates two complementary bulk heterojunctions (BHJs) (PDPP3T:PCBM and P3HT:PCBM), as shown in Figure 10d.[162] In particular, the PDPP3T:PCBM BHJ was used as the photoresponsive active layer and dominated the transient photoresponse behavior, while the P3HT:PCBM BHJ facilitated the subsequent electron trapping process at the P3HT:PCBM/PVA interface, determining the decay behavior of the device. These two BHJs synergistically modulate the channel carrier concentrations. As shown in Figure 10e, the device achieved a light-intensity-dependent active photoadaptation behavior and showed a higher current decay speed at higher light intensities. The potential of the device in simulating advanced visual adaptation was demonstrated by constructing a flexible 3 × 3 light-sensing array, which showed a higher background adaptation speed than the biological visual system (less than 2 s at 1 \times 10⁴ cd m⁻²) (Figure 10f,g).

Alternatively, in a three-terminal neuromorphic transistor, the visual adaptation functionality can be emulated via halide phase segregation or simple optoelectronic circuit integration. For example, Hong et al. reported a neuromorphic phototransistor comprising a hybrid architecture of CsPb(Br_{1-x}I_x)₃ perovskite and MoS₂.^[163] Interestingly, under continuous red-light irradiation, the phototransistor exhibited significant photocurrent degradation over time. Such an adaptive behavior can be attributed to light-driven halide phase segregation within the mixed CsPb(Br_{1-v}I_v)₃ perovskite, which leads to the creation of iodide- and bromide-rich regions. The generated bromide-rich phase widens the energy bandgap of the mixed perovskite, causing the photocurrent to decay over time under red light. The proposed adaptive phototransistor based on the halide-phase segregation mechanism provides an effective approach for realizing selective light-detection image sensors. Kwon et al. demonstrated a light-adjustable photoelectric neuromorphic integrated system that could simulate both the photopic and scotopic adaptations of the human retina. [164] The neuromorphic circuit comprised a

15214095, 0, Downloaded from https://advanced.onlinelibrary.wiley.com/doi/10.1002/adma.202505420 by HONG KONG POLYTECHNIC UNIVERSITY HU NG HOM, Wiley Online Library on [26/09/2025]. See the Terms

conditions) on Wiley Online Library for rules of use; OA articles are governed by the applicable Creative Commons I

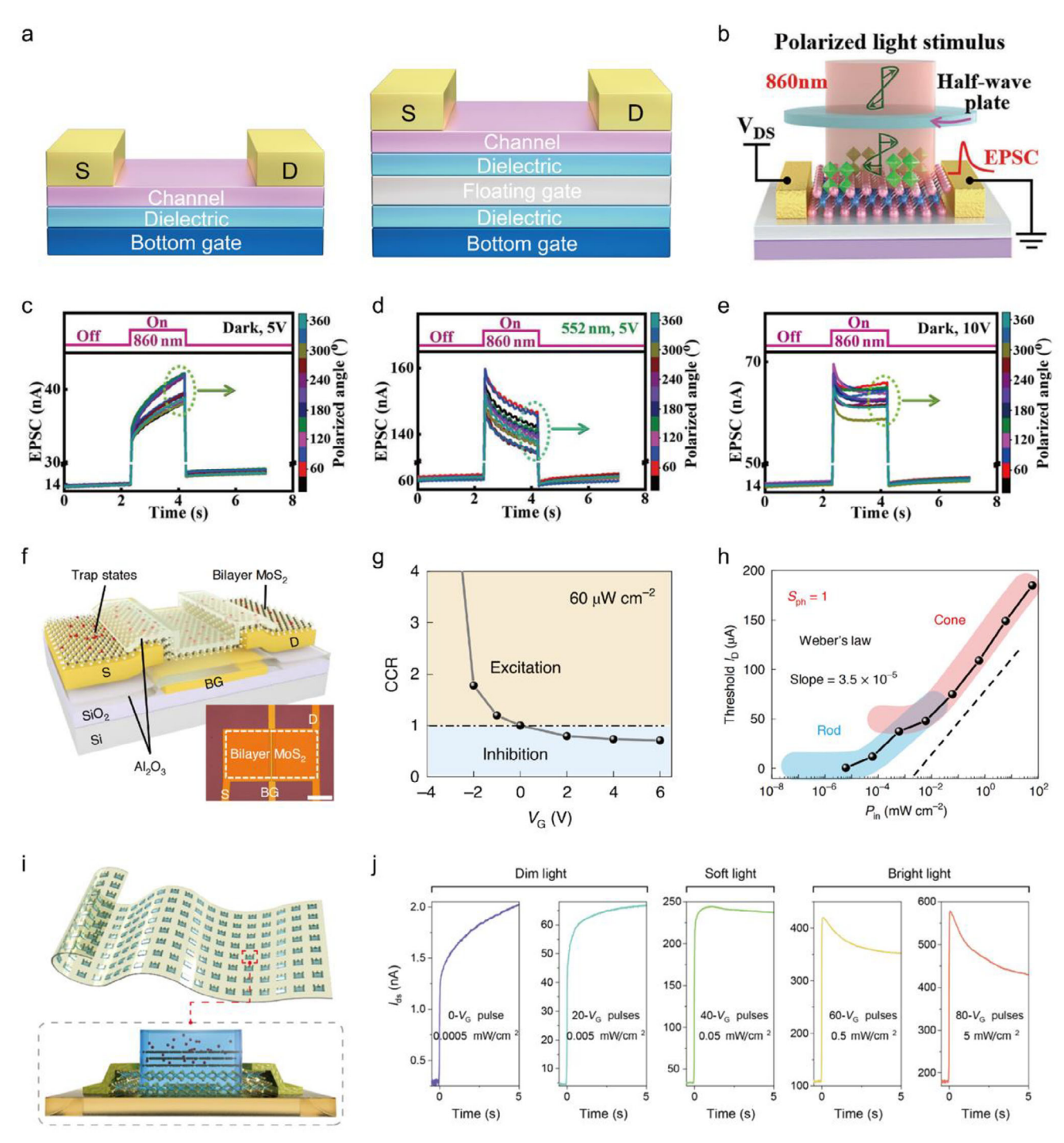


Figure 9. Bioinspired adaptive neuromorphic transistors with dynamic trapping in the channel layer: a) Schematic of two typical adaptive neuromorphic transistors. b) Schematic of a (UiO-66-NH₂)/ReS₂ heterojunction neuromorphic transistor. c) Time-dependent EPSC under a dark environment to different polarization angles with a fixed $V_{\rm Spike}$ of 5 V. d) Time-dependent EPSC under a green-light environment (light wavelength: 552 nm, light power: 20 mW cm⁻²) to different polarization angles with a fixed $V_{\rm Spike}$ of 5 V. e) Time-dependent EPSC in a dark environment to different polarization angles with a fixed $V_{\rm Spike}$ of 10 V. b—e) Reproduced with permission. (159) Copyright 2023, Wiley-VCH. f) Schematic of a MoS₂ phototransistor. Inset: the optical microscopy image of an individual MoS₂ phototransistor. g) Extracted current change ratio (CCR) at different $V_{\rm G}$ values. h) Threshold $I_{\rm D}$ as a function of incident power densities ($P_{\rm in}$). f-h) Reproduced with permission. (95) Copyright 2022, Springer Nature. i) Schematic of the flexible vision sensor array (top) and an individual vision sensor (bottom). j) Time-dependent photocurrent of a vision sensor after applying a different number of $V_{\rm G}$ pulses according to the light intensities. i,j) Reproduced under the terms of the CC-BY Creative Commons Attribution 4.0 International license (https://creativecommons. org/licenses/by/4.0). (161) Copyright 2024, The Authors, published by Wiley-VCH.

15214095, 0, Downloaded from https://advanced.onlinelibrary.wiley.com/doi/10.1002/adma.202505420 by HONG KONG POLYTECHNIC UNIVERSITY HU NG HOM, Wiley Online Library on [26/09/2025]. See the Terms

and-conditions) on Wiley Online Library for rules of use; OA articles are governed by the applicable Creative Commons I

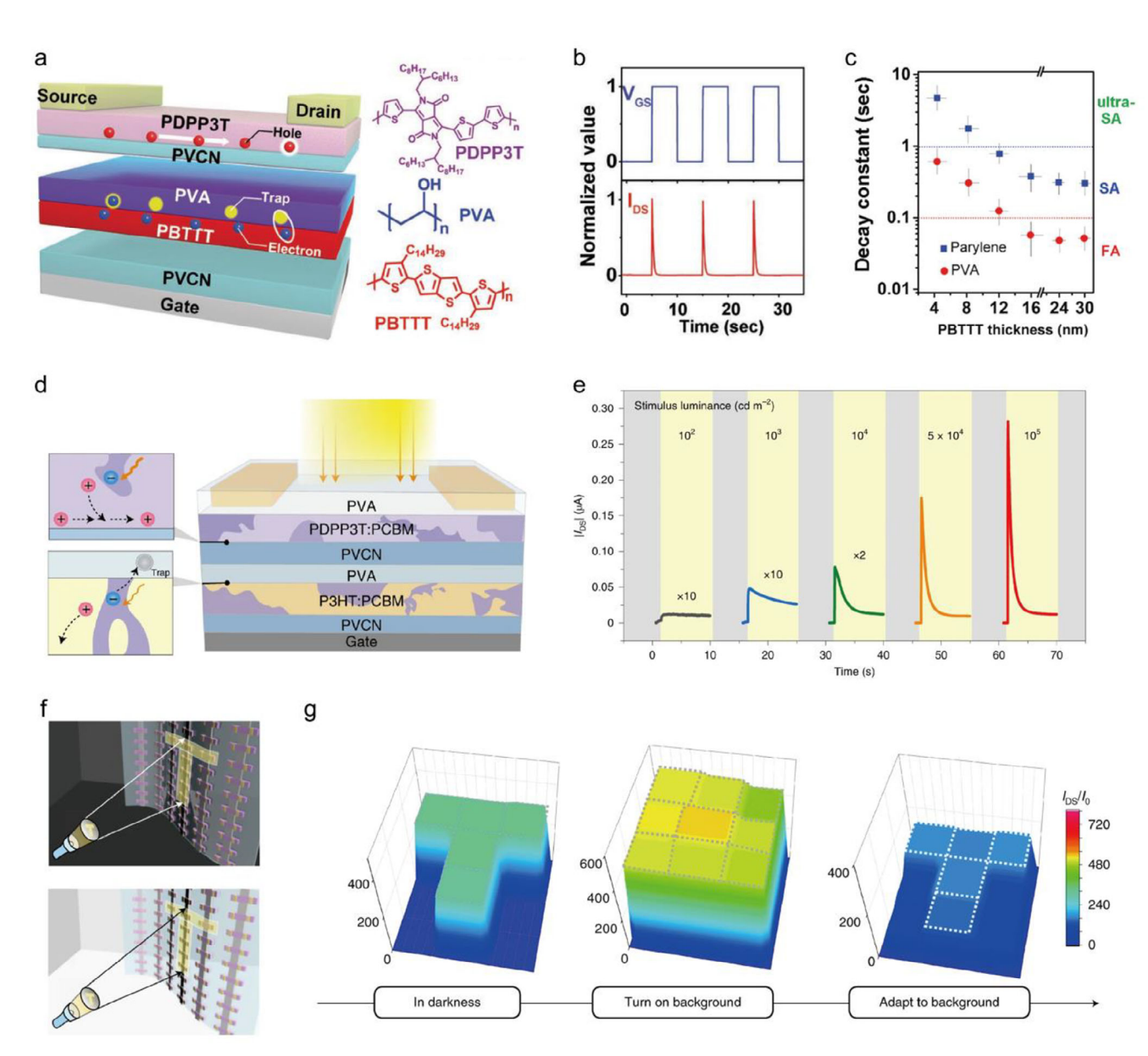


Figure 10. Bioinspired adaptive neuromorphic transistors with dynamic trapping in the dielectric layer. a) Device geometry of the organic adaptive transistor. b) Time-dependent I_{DS} ($V_{DS} = -1$ V) response of the device upon V_{CS} pulse (-4 V). c) Decay constants as a function of the PBTTT thickness with PVA or parylene charge trapping dielectrics. a–c) Reproduced with permission. [97] Copyright 2019, Wiley-VCH. d) Schematic of an organic active adaptation transistor with two complementary BHJs. e) Real-time photoresponse of the device under different illumination intensities. f) Schematic of the organic active adaptation transistor array in a dark background (top) and after switching to a bright background (bottom). g) Current mapping of the organic active adaptation transistor array under different conditions. d–g) Reproduced with permission. [162] Copyright 2021, Springer Nature.

photovoltaic divider (CdSe photosensor + IGZO load transistor) and an IGZO ionotronic synaptic transistor. The photovoltaic divider converts external light information into electrical signals, which play the role of an artificial retina, whereas the ionotronic synaptic transistor emulates the biological synaptic function and plays the role of an artificial optic nerve. In particular, the visual threshold of a device for ambient light intensity can be modulated by changing the load gate voltage (V_L). Under a strong background light, increasing V_L can improve the visual threshold and enable photopic adaptation. Under low-intensity background

lighting, reducing $V_{\rm L}$ can lower the visual threshold and facilitate scotopic adaptation.

4. Integrated Adaptive System for Biomimetic Applications

Recent advances in material and mechanism innovations, along with device structure design, have enabled the successful emulation of biological sensory adaptation using next-generation electronic devices, including piezoelectric and triboelectric sensors,



ADVANCED MATERIALS

www.advmat.de

memristors, and neuromorphic transistors. Unlike conventional sensors, these adaptive devices offer significant benefits such as superior high-frequency vibration detection, enhanced sensitivity to future stimulus variations, and a wider perceptual range. [95,97] Further integration of bio-inspired adaptive sensor arrays with data acquisition, signal processing, wireless transmission, and display modules can enable the construction of adaptive perception systems. These biologically inspired adaptive systems are expected to play a vital role in various intelligent applications such as electronic skins, wearable electronics, and machine vision.

4.1. Electronic Skin

The skin, which is a crucial medium for human interaction with the environment, can perceive external stimuli and transmit information to the brain. [165] Integrating skin-like sensory capabilities into robotics and prosthetics can help achieve smart grasping and accurate identification of daily objects as well as perform various challenging tasks. [166,167] For instance, Wu et al. designed a robotic manipulator integrated with a bimodal tactile sensor to simultaneously identify softness and texture features.^[107] Specifically, when the robotic manipulator touches samples with different elastic moduli, the bimodal sensor generates a piezoelectric response to predictively classify the softness and generate piezoresistive response to quantitatively detect softness (Figure 11a-c). By sliding, the bimodal sensor could perform texture recognition using spectral analysis and deep learning (Figure 11d,e). By leveraging this nondestructive and precise softness and texture measurement technology, the authors further integrated this bimodal sensor with multichannel data acquisition, signal processing, wireless transmission, and real-time display modules to construct a real-time visualized clinical feature recognition system. The system dynamically displayed the identification results of the neural network for healthy and pathological porcine mucosal features with an impressive accuracy of 98.44%. Wang et al. reported a memristor-based differential neuromorphic computing approach providing a neuromorphic-style sensory adaptation to environmental stimuli (Figure 11f).[168] This method exploits the intrinsic multiresistance characteristics of memristors. Based on the specific features of external stimuli, an adaptive memristive modulation scheme is used to adjust the memristor to remain at high (>250 kΩ), medium (\approx 170 kΩ), and low (<100 k Ω) resistance levels, which correspond to three biological sensory behaviors: adaptation, recovery, and nociception, respectively. In the task of grasping objects, this memristor-based adaptive perception method can identify and learn the key features of unknown objects and realize secure and stable grasping of sharp and slippery targets.

In a biological tactile skin system, analog receptor potentials are further converted into digital frequency signals, that is, action potentials, and are then transmitted along the sensory synapses to the central nervous system. To directly interface the electronic skin with nerve tissue, Chun et al. engineered a bio-inspired neural haptic sensing system by integrating a bimodal tactile sensor and a signal conversion circuit. A dual-mode tactile sensor was fabricated by combining piezoresistive rGO sheets and piezoelectric BaTiO₃ nanoparticles in a polymeric PDMS matrix. The signal conversion system comprises four key compo-

nents: readout circuits for rapidly and slowly adapting sensors, an analog-to-digital converter, a central processing unit, and a neural stimulator circuit. It is used to transform the electrical output of a sensor into sensory-neuron-mimicking pulse signals based on real response patterns from slowly and rapidly adaptive mechanoreceptors. Animal experiments have shown that the generated pulse output signal can complete transmission in an explanted afferent tactile nerve while simultaneously eliciting efferent nerve stimulation in mice, resulting in muscle contraction of the hind limbs. These findings have significant implications for advancing neural prosthetics, biomimetic robotics, and human-machine interface technologies (Figure 11g,h). Do et al. designed a self-powered piezotronic artificial mechanoreceptor by integrating a piezoelectric tactile sensor with a synaptic ionogel-gated field-effect transistor.^[170] The tactile sensor was composed of high-performance piezoelectric nanocomposites of P(VDF-TrFE)/modified-BaTiO₃ nanoparticles. A synaptic transistor was fabricated using p-type rGO as the channel and an ionogel as the gate dielectric. On applying mechanical stimulation to the tactile sensor, the integrated device could convert the piezoelectric potential generated by the sensor into a synaptic current output with short-term plasticity and long-term plasticity and effectively recognize and memorize pressure information.

4.2. Wearable Electronics

As a wearable electronic device, an integrated adaptive system can provide multifunctional capabilities, including motion monitoring, health management, and human-machine interaction.[171,172] Xiong et al. reported a high-performance PVDF-based composite nanofiber piezoelectric membrane for wearable physical monitoring applications.[173] This innovative membrane features a hierarchical architecture comprising PVDF/dopamine (DA) nanofiber membranes integrated with ultrafine PVDF/DA nanofibers to form a continuous and homogeneously distributed 2D network structure. The optimized configuration endows the composite with remarkable piezoelectric properties, demonstrating a wide detection range (1.5-40 N), remarkable sensitivity (7.29 V N⁻¹ in the 0–4 N regime), and exceptional cyclic stability (>10 000 operation cycles). The outstanding performance and intrinsic flexibility of the membrane enable it to serve as a flexible wearable sensor that can be employed to track human movements, such as elbow bending, finger tapping, knee bending, and foot stamping, as well as subtle physiological cues, such as speech patterns and wrist pulses (Figure 12a). Fang et al. proposed a triboelectric sensor network embedded in masks to monitor respiratory patterns in real time (Figure 12b).[174] The sensor, composed of breathable and moisture-resistant textile materials featuring spindle-knotted fibers induced by Rayleigh instability, exhibited a rapid response time (0.28 s), robust signalto-noise ratio (51.2 dB), and superior sensitivity (0.46 V kPa⁻¹). Using computational fluid dynamics simulations, the authors optimized the distribution of sensor networks to enhance the detection fidelity during respiratory monitoring. Simultaneously, a 1D convolutional neural network was applied to recognize respiratory patterns, achieving an exceptional classification accuracy of 100%. Furthermore, a wireless respiratory monitoring system was built by integrating the on-mask sensor network with a

15214095, 0, Downloaded from https://advanced.onlinelibrary.wiley.com/doi/10.1002/adma.202505420 by HONG KONG POLYTECHNIC UNIVERSITY HU NG HOM, Wiley Online Library on [2609/2025]. See the Terms and Conditions (https://onlinelibrary.wiley.com/doi/10.1002/adma.202505420 by HONG KONG POLYTECHNIC UNIVERSITY HU NG HOM, Wiley Online Library on [2609/2025]. See the Terms and Conditions (https://onlinelibrary.wiley.com/doi/10.1002/adma.202505420 by HONG KONG POLYTECHNIC UNIVERSITY HU NG HOM, Wiley Online Library on [2609/2025]. See the Terms and Conditions (https://onlinelibrary.wiley.com/doi/10.1002/adma.202505420 by HONG KONG POLYTECHNIC UNIVERSITY HU NG HOM, Wiley Online Library on [2609/2025]. See the Terms and Conditions (https://onlinelibrary.wiley.com/doi/10.1002/adma.202505420 by HONG KONG POLYTECHNIC UNIVERSITY HU NG HOM, Wiley Online Library on [2609/2025]. See the Terms and Conditions (https://onlinelibrary.wiley.com/doi/10.1002/adma.202505420 by HONG KONG POLYTECHNIC UNIVERSITY HU NG HOM, Wiley Online Library on [2609/2025].

and-conditions) on Wiley Online Library for rules of use; OA articles are governed by the applicable Creative Commons I

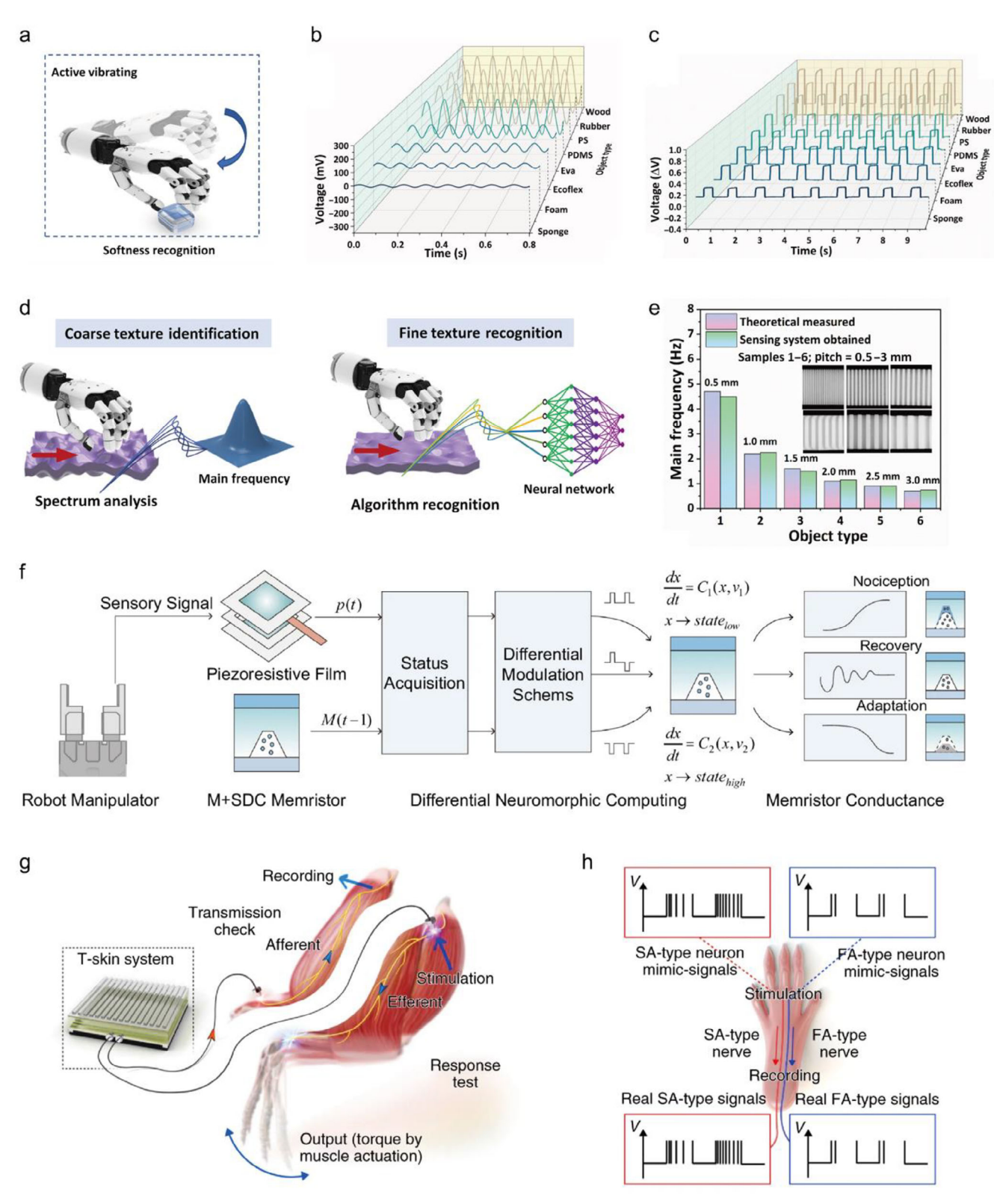


Figure 11. Integrated adaptive system for electronic skin: a) Schematic of softness recognition of a robotic manipulator using active vibrating motion. b) Real-time piezoelectric output of the piezoelectric mode when touching eight objects. c) Relative voltage changes in the piezoesistive mode when the robotic manipulator applies pressure onto eight objects. d) Schematic of identifying coarse texture by spectral analysis and identifying fine texture by an artificial neural network. e) Comparison of the main frequency from six 3D-printed samples with spacings ranging from 0.5 to 3 mm between theoretical analysis and experimental demonstrations. a—e) Reproduced under the terms of the CC-BY Creative Commons Attribution 4.0 International





wearable signal processing unit, Bluetooth wireless transmission module, and dedicated smartphone application (Figure 12c,d).

To bridge the communication gap between non-signing individuals and people with auditory/verbal disabilities, Wen et al. designed a comprehensive sign language interpretation system featuring three key components: a triboelectric sensor-embedded smart glove, an artificial intelligence (AI) processing module, and a virtual reality (VR) interface.[175] The glove subsystem incorporated 15 flexible triboelectric sensors with a multi-layer structure (conductive textile/ecoflex/wrinkled nitrile/conductive textile) strategically positioned at key hand joints and finger segments to capture comprehensive gesture data. The AI architecture demonstrates robust performance through dual-processing frameworks: 1) a non-segmented model achieving an recognition accuracy of 91.3% on 50 words and a recognition accuracy of 95% on 20 sentences, and 2) a segmented approach enabling generalization to new/never-seen sentences with an average recognition accuracy of 86.67%. Real-time translation of recognized sign language occurs through the VR interface, which renders instantaneous text displays and synthetic voice outputs, creating bidirectional communication channels between sign language users and non-signers. Pang et al. further advanced wearable technology by engineering a textile-based multifunctional tactile sensor system for human-machine interfacing.[176] This innovative design biomimetically replicates two distinct cutaneous mechanoreceptor functions: fast-adapting responses through a triboelectric layer (Teflon-steel yarns on a cotton textile) and slowadapting responses via a piezoresistive layer (carbon-nanotubeembedded textile) (Figure 12e). Owing to its dual-sensing capabilities, the device demonstrated remarkable versatility in perceiving complex mechanical stimuli, ranging from physiological signals (vocal vibrations and arterial pulse waveforms) to dynamic joint kinematics (elbow, wrist, and knee flexion). To enable intuitive manipulation of soft robotic grippers, the sensor array was seamlessly interfaced with an embedded processing and data communication module, forming a complete wearable interface platform for precise motion control applications (Figure 12f). As shown in Figure 12g, the wrist flexion triggers the generation of a continuous current signal that proportionally regulates the bending motion of the robotic arm. Notably, the robotic gripper executes grasping/releasing operations through triboelectric signals activated by the finger pressure on the sensor, thereby achieving pressure-dependent object manipulation.

Gas sensors, which serve as key elements in electronic skin and wearable electronics, have shown great promise for applications in health monitoring and environmental perception over the past few years. By integrating flexible substrates with nanosensitive materials (such as metal oxide semiconductors, conductive polymers, and 2D transition metal dichalcogenides), next-generation gas sensors can achieve high sensitivity, rapid response, and low power consumption. These advancements enable the real-time detection of volatile organic compounds (e.g.,

acetone and ammonia) in human breath or hazardous gases (e.g., carbon monoxide and nitrogen dioxide) in the environment, providing critical data for early disease diagnosis (e.g., diabetes and lung cancer) and air quality assessment.[177–179]

4.3. Machine Vision

Machine vision systems designed to mimic biological mechanisms for real-time monitoring and identification are crucial components employed in diverse intelligent applications such as autonomous vehicles, biomimetic robots, industrial manufacturing, and security surveillance. [180,181] However, existing systems typically exhibit a narrow dynamic range (60–70 dB) coupled with a fixed spectral response, which significantly hinders their performance in obtaining high-quality images in challenging lighting conditions. [95] In recent years, several bioinspired visual adaptation strategies have been implemented to enhance the light capture and image quality at sensory terminals. Based on their distinct operational principles, these strategies are primarily classified into two fundamental categories: bioinspired light-intensity adaptation and bioinspired spectral adaptation.

4.3.1. Bioinspired Light-Intensity Adaptation

Machine vision systems must encode scenes across a broad spectrum of lighting conditions. Precise image acquisition under varying illumination intensities is fundamental to reliable environmental perception and accurate object recognition. Inspired by the visual adaptation functionality of the human retina, Gong et al. designed an array of antagonistic photovoltaic memristors that can simulate visual photopic, scotopic, and contrast adaptations (Figure 13a).[94] The incorporation of two antagonistic photovoltaic junctions—a Schottky junction (ITO/MAPbI₃) and a p-n junction (P3HT/MAPbI₃)—contributes to eliciting dynamic photocurrent responses under different illumination intensities in a single device (Figure 13b). When exposed to dim lighting conditions, the ITO/MAPbI₃ Schottky junction primarily governs the photovoltaic direction, and the device exhibits a positive photocurrent. Under a high light intensity, light-induced doping leads to an increase in the built-in electric field at the asymmetric p-n junction. In this case, the p-n junction dominates the photovoltaic direction, and the device photocurrent switches from positive to negative. In particular, the light-intensity-dependent switchable photovoltaic characteristics conformed to Weber's law, demonstrating an inverse proportionality between photosensitivity and light stimulus intensity (Figure 13c). The photomemristor array showed exceptional performance in encoding high-contrast scenes with a dynamic range extending to 94 dB, while achieving active adaptation speeds below 1.2 s, significantly surpassing the capabilities of the human visual system (Figure 13d).

License (http://creativecommons.org/licenses/by/4.0/).[107] Copyright 2024, The Authors, Published by American Association for the Advancement of Science. f) Utilizing differentiation processing method to process tactile information and mimic multiple receptors; Reproduced under the terms of the CC-BY Creative Commons Attribution 4.0 International License (http://creativecommons.org/licenses/by/4.0/).[168] Copyright 2024, The Authors, Published by Springer Nature. g) Schematic describing two animal experiments. h) Stimulation and recording in slow adaptive and rapid adaptive nerves. g,h) Reproduced with permission.[169] Copyright 2021, Springer Nature.

15214095, 0, Downloaded from https://advanced.onlinelibrary.wiley.com/doi/10.1002/adma.202505420 by HONG KONG POLYTECHNIC UNIVERSITY HU NG HOM, Wiley Online Library on [2609/2025]. See the Terms and Conditions (https://onlinelibrary.wiley.com/doi/10.1002/adma.202505420 by HONG KONG POLYTECHNIC UNIVERSITY HU NG HOM, Wiley Online Library on [2609/2025]. See the Terms and Conditions (https://onlinelibrary.wiley.com/doi/10.1002/adma.202505420 by HONG KONG POLYTECHNIC UNIVERSITY HU NG HOM, Wiley Online Library on [2609/2025]. See the Terms and Conditions (https://onlinelibrary.wiley.com/doi/10.1002/adma.202505420 by HONG KONG POLYTECHNIC UNIVERSITY HU NG HOM, Wiley Online Library on [2609/2025]. See the Terms and Conditions (https://onlinelibrary.wiley.com/doi/10.1002/adma.202505420 by HONG KONG POLYTECHNIC UNIVERSITY HU NG HOM, Wiley Online Library on [2609/2025]. See the Terms and Conditions (https://onlinelibrary.wiley.com/doi/10.1002/adma.202505420 by HONG KONG POLYTECHNIC UNIVERSITY HU NG HOM, Wiley Online Library on [2609/2025].

com/terms-and-conditions) on Wiley Online Library for rules of use; OA articles are governed by the applicable Creative Commons License

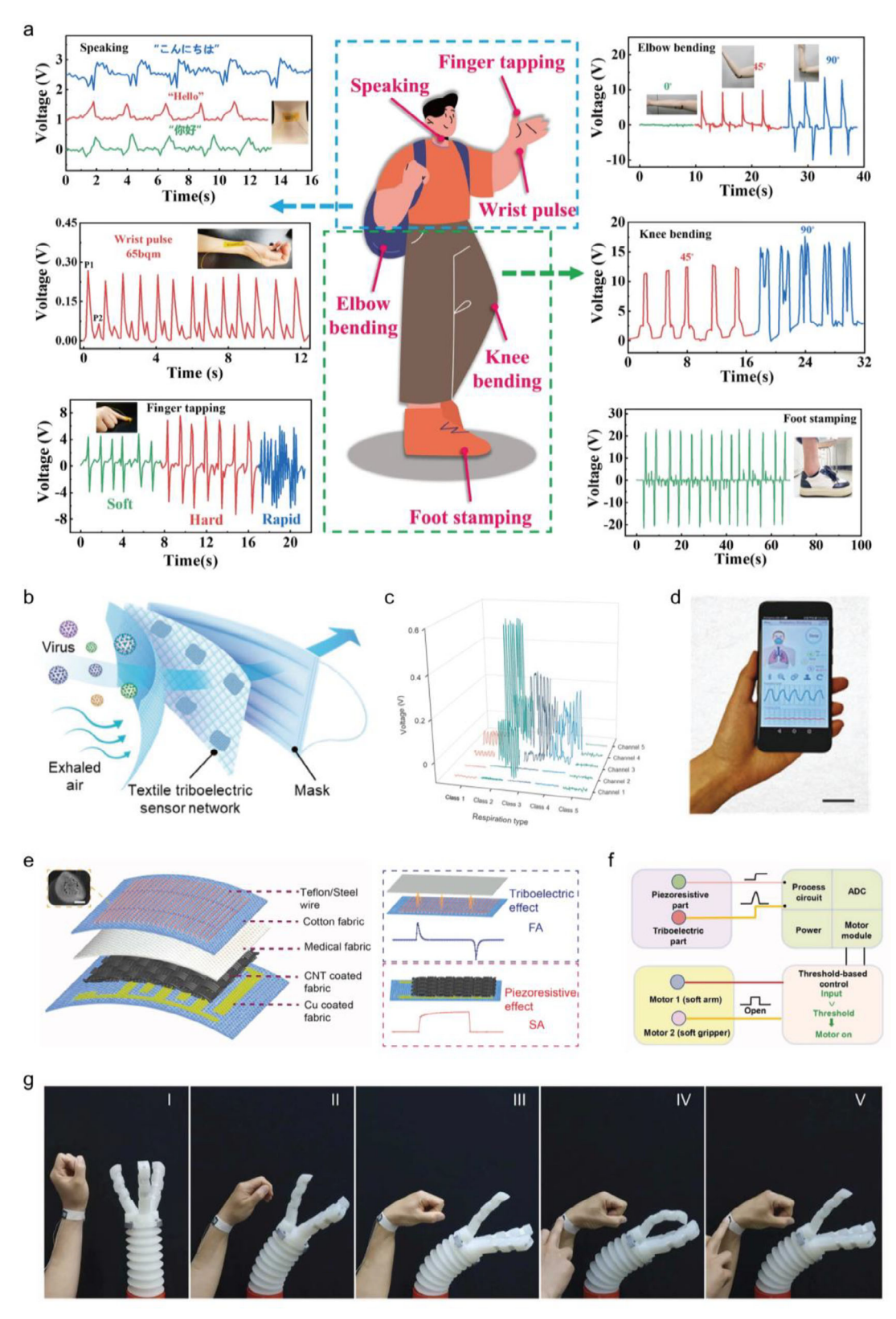


Figure 12. Integrated adaptive system for wearable electronics: a) Real-time monitoring of human motions and subtle physiological activities, including speaking, wrist pulse, finger tapping, elbow bending, knee bending, and foot stamping; Reproduced under the terms of the CC-BY Creative Commons Attribution 4.0 International License (http://creativecommons.org/licenses/by/4.0/). [173] Copyright 2024, The Authors, Published by Springer Nature. b) Design of an on-mask sensor network. c) Corresponding five-channel output spectra of the collected typical respiratory signals as the input of the

ADVANCED MATERIALS

www.advmat.de

Li et al. demonstrated a biomimetic avalanche transistor based on a MoS₂/WSe₂ van der Waals heterostructure that can mimic the feed-forward inhibition circuit in the retina and realize ultrafast visual adaptation at the microsecond level.[182] With increasing light intensity, the primary mechanism responsible for photocurrent generation shifts from the highly sensitive avalanche effect to the less-sensitive photoconductive effect. This behavior is similar to the light-intensity-dependent transition between the rod and cone photoreceptors in the retinal system. With the avalanche tuning operation, the device can achieve ultra-fast and high-frequency scotopic (108 µs and 6 kHz) and photopic (268 us and 3 kHz) adaptations. An adaptive machine vision system that integrates biomimetic avalanche transistors with artificial neural networks was developed. The system exhibited excellent microsecond-level fast adaptability and powerful image recognition ability with an accuracy of over 98% under both dim and bright conditions (Figure 13e,f). To meet the multifunctional requirements of next-generation wearable and implantable electronics, Wang et al. engineered an intrinsically stretchable visual adaptive phototransistor based on viscoelastic perovskite films.[183] Specifically, CsPbBr₃ perovskite QDs were distributed in a SEBS elastomer in the form of quasi-continuous microspheres using a surface energy induction strategy. The resulting device exhibited trichromatic photoadaptation and high biaxial stretchability (up to 100%). The visual adaptation functionality was further demonstrated by attaching a phototransistor pixel to the ocular prosthesis. For scotopic adaptation, the phototransistor pixel drives the light-emitting diode (LED) from dark to bright. For photopic adaptation, the phototransistor pixel drives the LED from bright to dark (Figure 13g).

4.3.2. Bioinspired Spectral Adaptation

The natural spectrum has a wide range of wavelengths. Visual information encoded in distinct spectral regions undergoes dynamic variations in response to environmental changes. To capture high-fidelity images in spectrally variable scenes, some creatures in nature, such as the Pacific salmon (Oncorhynchus keta), have evolved a spectra-adapted vision mechanism.[184] Such a visual adaptation mechanism can dynamically adjust the retinal spectral sensitivity to align with the prevailing wavelengths in the ambient environment.[185] To mimic the spectral adaptation behavior of Pacific salmon, Ouyang et al. designed a visual sensor incorporated with two back-to-back p-n photovoltaic junctions, exhibiting distinct spectral response patterns under varying bias voltages.[186] As shown in Figure 14a, the device architecture features a multilayer configuration comprising ITO/n-type titanium dioxide (n-TiO₂)/p-type antimony selenide (p-Sb₂Se₃)/n-type silicon (n-Si)/Ag. When a positive bias was applied to the ITO electrode, the shallow TiO₂/Sb₂Se₃ junction dominated the photocurrent direction, and the device exhibited a broadband visible spectrum response. When a negative bias was applied to the ITO electrode, the bottom deep $\mathrm{Sb}_2\mathrm{Se}_3/\mathrm{Si}$ junction dominated the photocurrent direction, and the device exhibited a narrowband near-infrared spectrum response (Figure 14b). Notably, the bioinspired visual sensor could operate at frequencies as high as 100 kHz, matching the frame-rate performance of cutting-edge commercial optical sensors (Figure 14c). An 8×8 image sensor array was used to further demonstrate the dynamic spectral adaptation function. The results indicate that the spectral adaptation process significantly improves the image quality, achieving more than a tenfold enhancement in the Weber contrast for the captured images (Figure 14d,e).

Based on oxygen-mediated 2D platinum diselenide (PtSe₂), Tan et al. reported a bioinspired retinomorphic two-terminal device exhibiting nonvolatile bipolar photoconductivity with wavelength-dependent characteristics.[187] Specifically, under short-wavelength (450 nm) and medium-wavelength (532 nm) light pulses, the detachment of oxygen molecules bound to the surface of the bilayer PtSe2 leads to a negative photocurrent response, whereas under long-wavelength (650 nm) light pulses, the physisorption of oxygen molecules leads to a positive photocurrent response. The proposed retinomorphic device could spontaneously form antagonistic receptive fields (red-blue and red-green). Compared with an independent pseudocolor channel (less than 75%), the bio-inspired visual sensor showed a higher image classification accuracy (93.55%) (Figure 14f,g). Mathews et al. developed a self-powered perovskite bipolar photodetector with a tandem p-i-n-i-p structure (ITO/PEDOT:PSS/FA_{1.05}PbBr₃/PCBM/MAPbI₃/Spiro/Au).^[188] The device utilized two types of perovskite materials with different bandgaps as intrinsic absorption layers. The wide-bandgap perovskite FA_{1.05}PbBr₃ absorbs short-wavelength light and generates a negative photocurrent. Narrow-bandgap perovskite MAPbI₃ absorbs long-wavelength light and generates a positive photocurrent. Such bipolar photoresponse behavior can achieve two perceptually significant chromatic opponent channels (redgreen and yellow-blue). With the use of chromatic opponent channels, red adaptation and brightness adaptation can be simulated by adjusting the photoresponsivity to red light or red light and green light, respectively (Figure 14h).

5. Challenges and Outlooks

Unlike conventional sensors with stable signal outputs, biological sensory neurons can adapt dynamically to varying environments, providing a highly efficient neural encoding strategy. Over the past decade, significant advancements have been made in the development of sensory adaptation-inspired devices involving new materials, novel mechanisms, and innovative device geometries, which are expected to help implement high-performance neuromorphic sensing systems in the future. Despite the progress in the basic science and application of bioinspired adaptive sensors, many challenges remain, including

convolutional neural network. d) Image for real-time wireless respiratory monitoring and management using a customized cellphone application. b–d) Reproduced with permission. [174] Copyright 2022, Wiley-VCH. e) Left: detailed structure of the textile tactile sensor. Right: schematics and representative output signals of the triboelectric sensor layer (top) and piezoresistive sensor layer (bottom) when subjected to pressure force. f) Schematic of the remote soft robotic control system using the tactile sensor as a human–machine interface. g) Images of the soft robotic manipulator and human arm under different control commands controlled by the sensor. e–g) Reproduced with permission. [176] Copyright 2022, Elsevier.

15214095, 0, Downloaded from https://adanced.onlinelibrary.wiley.com/doi/10.1002/adma.202505420 by HONG KONG POL YTECHNIC UNIVERSITY HU NG HOM, Wiley Online Library on [26092025]. See the Terms and Conditions (https://onlinelibrary.wiley)

conditions) on Wiley Online Library for rules of use; OA articles are governed by the applicable Creative Commons I

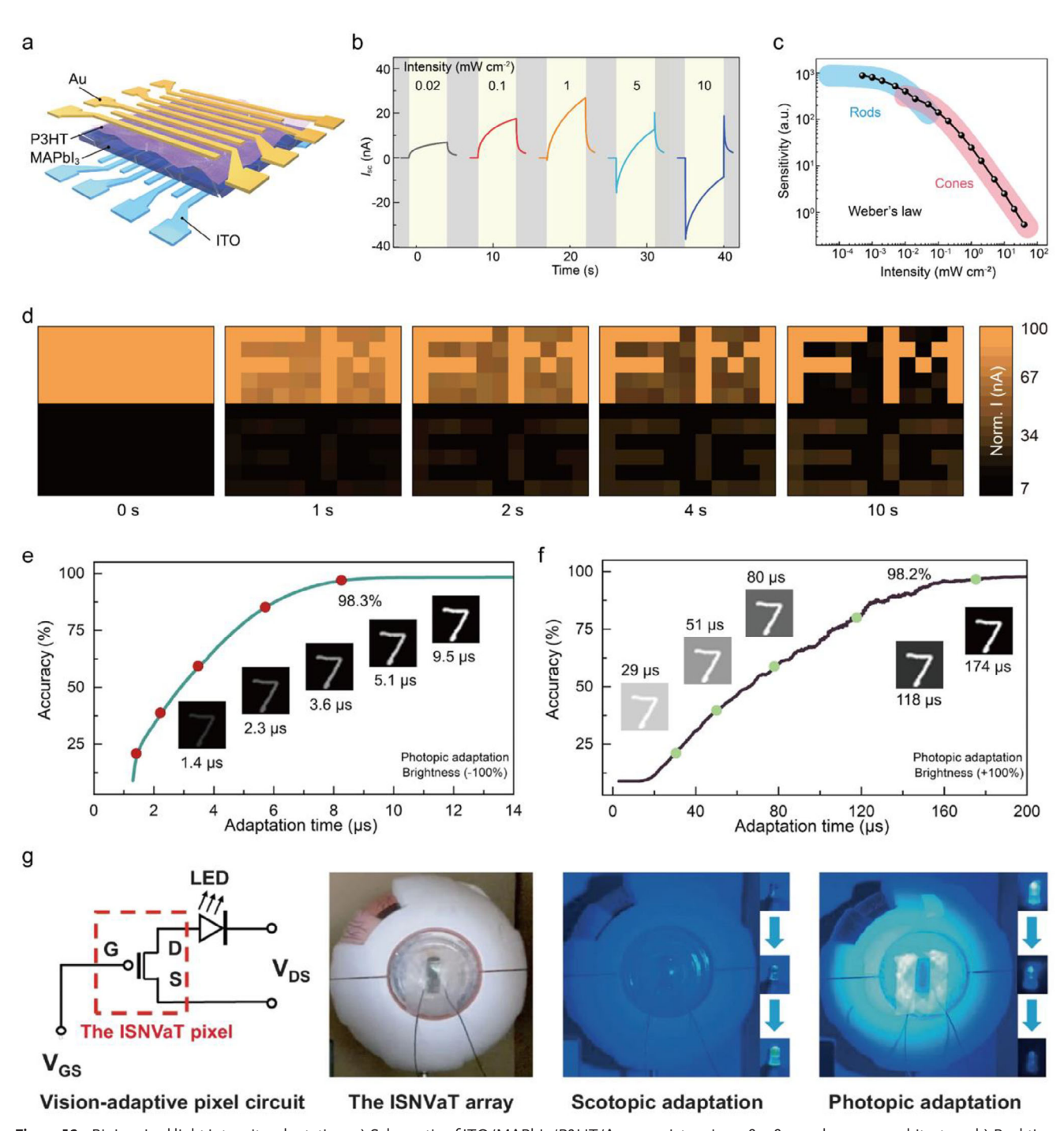


Figure 13. Bioinspired light intensity adaptation: a) Schematic of ITO/MAPbl₃/P3HT/Au memristors in an 8 × 8 crossbar array architecture. b) Real-time photoresponse of the memristor under illumination with varied light intensities. c) Relationship between photosensitivity and light intensity. d) Time course of active contrast adaptation for the high-contrast "FMEG" image. a–d) Reproduced under the terms of the CC-BY Creative Commons Attribution 4.0 International license (https://creativecommons.org/licenses/by/4.0). [94] Copyright 2024, The Authors, published by Wiley-VCH. e) Recognition rate of adaptative machine vision as a function of time for scotopic adaptation. f) Recognition rate of adaptative machine vision as a function of time for photopic adaptation. e,f) Reproduced under the terms of the CC-BY Creative Commons Attribution 4.0 International License (http://creativecommons.org/licenses/by/4.0/). [182] Copyright 2024, The Authors, Published by Springer Nature. g) Visual adaptation of the phototransistor pixel serving as an LED driver; Reproduced under the terms of the CC-BY Creative Commons Attribution 4.0 International License (http://creativecommons.org/licenses/by/4.0/). [183] Copyright 2024, The Authors, Published by Springer Nature.

15214955, 0, Downloaded from https://adarceed.onlinelibrary.wiley.com/doi/10.1002/adma.202505420 by HONG KONG POL YTECHNIC UNIVERSITY HU NG HOM, Wiley Online Library on [26/09/2025]. See the Terms and Conditions (https://onlinelibrary.wiley.com/doi/10.1002/adma.202505420 by HONG KONG POL YTECHNIC UNIVERSITY HU NG HOM, Wiley Online Library on [26/09/2025]. See the Terms and Conditions (https://onlinelibrary.wiley.com/doi/10.1002/adma.202505420 by HONG KONG POL YTECHNIC UNIVERSITY HU NG HOM, Wiley Online Library on [26/09/2025]. See the Terms and Conditions (https://onlinelibrary.wiley.com/doi/10.1002/adma.202505420 by HONG KONG POL YTECHNIC UNIVERSITY HU NG HOM, Wiley Online Library on [26/09/2025]. See the Terms and Conditions (https://onlinelibrary.wiley.com/doi/10.1002/adma.202505420 by HONG KONG POL YTECHNIC UNIVERSITY HU NG HOM, Wiley Online Library on [26/09/2025]. See the Terms and Conditions (https://onlinelibrary.wiley.com/doi/10.1002/adma.202505420 by HONG KONG POL YTECHNIC UNIVERSITY HU NG HOM, Wiley Online Library on [26/09/2025]. See the Terms and Conditions (https://onlinelibrary.wiley.com/doi/10.1002/adma.202505420 by HONG KONG POL YTECHNIC UNIVERSITY HU NG HOM. Wiley Online Library on [26/09/2025]. See the Terms and Conditions (https://onlinelibrary.wiley.com/doi/10.1002/adma.202505420 by HONG KONG POL YTECHNIC UNIVERSITY HU NG HOM Wiley Online Library.

and-conditions) on Wiley Online Library for rules of use; OA articles are governed by the applicable Creative Commons I

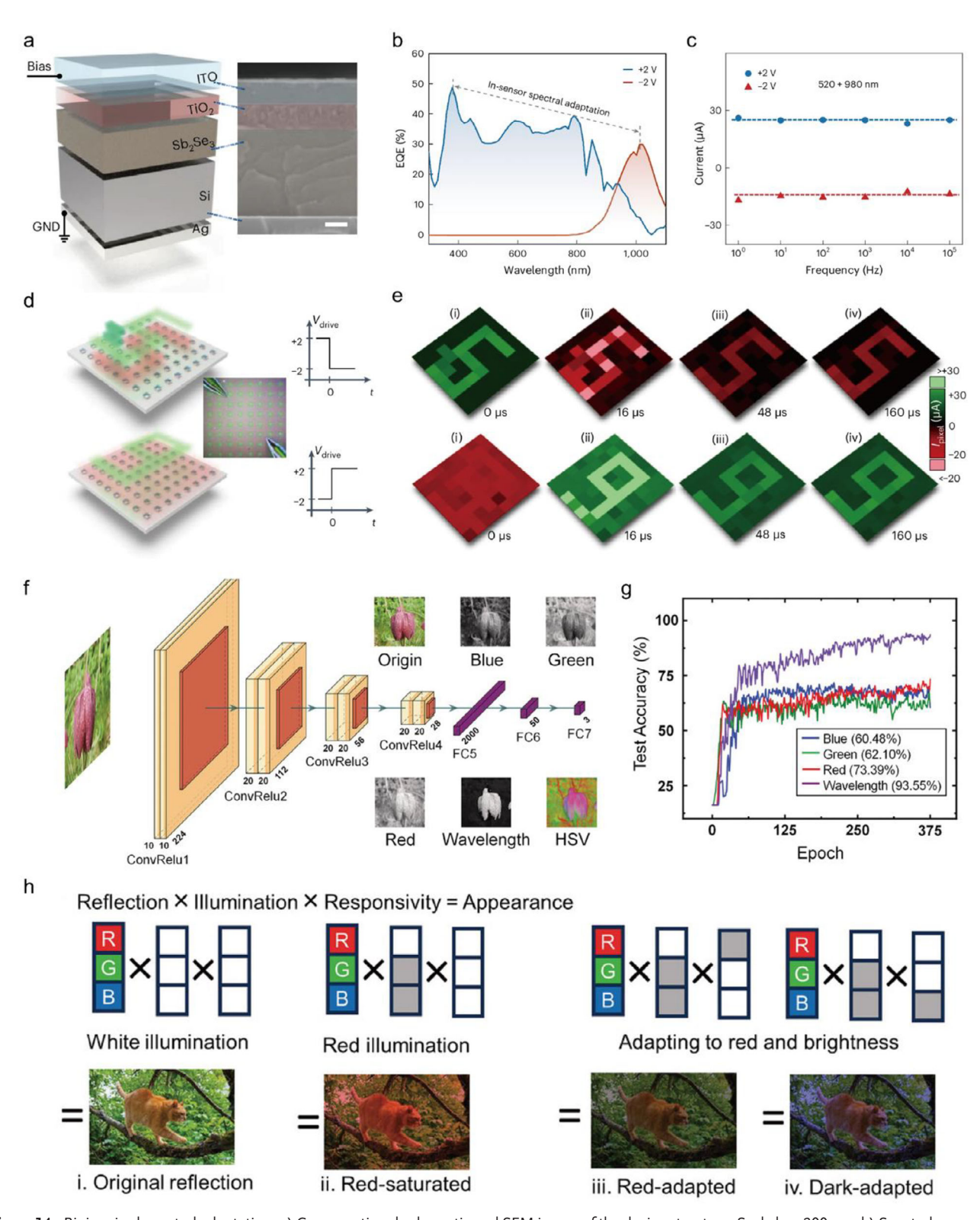


Figure 14. Bioinspired spectral adaptation: a) Cross-sectional schematic and SEM image of the device structure. Scale bar, 200 nm. b) Spectral response of a back-to-back photodiode under different bias voltages. c) Output current as a function of the frequency of bias voltage. d) Illustration of an 8 × 8 spectra-adapted vision sensor array in the near-infrared-spectrum and visible-spectrum adaptation test. e) Time course of the imaging result. a—e) Reproduced with permission. [186] Copyright 2024, Springer Nature. f) Convolutional neural network structure and different datasets. g) Classification results of four datasets under the same network structure. f,g) Reproduced with permission. [187] Copyright 2022, Wiley-VCH. h) Simulation of red and brightness self-adaptation in a bipolar photodetector; Reproduced with permission. [188] Copyright 2024, Wiley-VCH.



ADVANCED MATERIALS

vww.advmat.de

device performance optimization, multimodal adaptive sensors, and system-level integration.

- 1) Device performance optimization. Piezoelectric and triboelectric sensors exhibit inherent susceptibility to ambient environmental factors, such as temperature and humidity during routine operations, potentially leading to compromised device sensitivity. For example, when triboelectric sensors operate in extremely hot or humid environments, electron transfer occurs within the electrification layers. This phenomenon degrades the electrical output performance of the sensors, thereby compromising the accuracy of the output voltage measurement via the triboelectric mechanism.[119] For piezoelectric sensors, elevated temperatures can reduce the piezoelectric coefficients of the material, weaken the internal polarization, and degrade the sensitivity. Moreover, prolonged exposure to high temperatures exacerbates fatigue degradation, leading to decreased service life.[102,103] The implementation of reliable packaging technologies is imperative for minimizing the impact of external environmental conditions on device performance. Furthermore, piezoelectric materials may experience gradual performance degradation due to material fatigue during prolonged operation. The operational principle of triboelectric sensors, which is rooted in the interfacial charge transfer dynamics during surface contact-separation cycles, inevitably triggers mechanical abrasion at material interfaces, thereby compromising their long-term operational reliability. Ionic memristors exhibit significant variability in their resistive switching parameters owing to the stochastic formation and disruption of conductive filaments. With the doping of a resistive switching layer with non-metallic QDs (such as graphene oxide and PbS), conductive filaments can be directed to form at specific positions. The confinement effect of the localized electric fields of QDs regulates the growth path of the filaments, effectively suppressing the stochastic behavior.[189,190] Prolonged cycling can induce interface delamination or electrode fatigue through volumetric expansion or phase transitions caused by repetitive ion insertion/extraction processes. For three-terminal neuromorphic transistors, the primary challenge in developing adaptive devices lies in achieving a precise regulation of the electrontrapping processes within the channel or dielectric layers to realize on-demand charge confinement capabilities. Addressing these fundamental limitations requires a holistic approach that integrates material selection, interface engineering, fabrication processes, and device architecture through coordinated design optimization.
- 2) Multimodal adaptive sensors. All five classical senses—vision, hearing, touch, smell, and taste—exhibit sensory adaptation characteristics. However, current artificial adaptive sensors have predominantly focused on achieving adaptation functions in single modalities such as tactile or visual adaptation. Constrained by their transduction mechanisms, triboelectric and piezoelectric sensors are primarily limited to simulating tactile adaptation. A promising strategy for developing next-generation multimodal adaptive sensors is to utilize emerging devices, such as memristors or neuromorphic transistors, as adaptive processing units coupled with their integration with conventional sensing components. Sensory

- adaptation in biological systems is an intricate process involving multiple ionic species. Distinct sensory modalities exhibit varying adaptation timescales, ranging from milliseconds to tens of seconds. To effectively replicate the multimodal sensing capabilities of biological sensory systems, it is imperative to investigate multi-ion systems in ionic memristors while achieving precise spatiotemporal control over ion migration and diffusion processes. For three-terminal neuromorphic transistors, achieving a rational design and precise control of the defect energy levels is crucial. Moreover, multimodal sensor signals can be integrated using both neuromorphic hardware and neural networks. At the hardware level, Liu et al. developed a multimodal fusion-spiking neuron based on NbO, memristors.[191] This artificial neuron could simultaneously perceive pressure and temperature information by integrating and compressing multimodal signals through spike sequences. At the neural network level, the core of multimodal sensor signal fusion lies in the design of model architectures capable of effectively integrating heterogeneous modalities (e.g., vision, touch, and hearing). For example, intermediate fusion strategies employ attention mechanisms (such as intramodal self-attention and cross-modal attention) to dynamically weigh features across different modalities, thereby enhancing a model's ability to capture critical information. [192]
- System-level integration. System-level integration of multimodal adaptive sensing systems requires coordinated breakthroughs across hardware, algorithms, and architectural dimensions. At the hardware level, device-to-device variability remains a critical challenge that severely impedes the development of large-area high-density device arrays with exceptional uniformity. Furthermore, multimodal sensors typically incorporate devices based on diverse physical principles (e.g., pressure, chemical, and optical sensors), presenting significant compatibility challenges in material selection, fabrication processes, and interface standardization. From an algorithmic perspective, multimodal systems must effectively integrate heterogeneous information from various modalities (text, images, speech, video, etc.); however, substantial disparities in data structures across modalities pose challenges in feature extraction and semantic alignment. With increasing architectural complexity, multimodal neural networks are capable of unifying feature extraction, feature fusion, and decisionmaking within a single model. Currently, mainstream multimodal data fusion models can be categorized into five types: encoder-decoder methods, attention mechanism, generative neural networks, graph neural networks, and other constraint-based approaches. In the encoder-decoder framework, multimodal fusion is completed as follows. First, the encoder acts as a high-level feature extractor, projecting multimodal input data into a latent space with relatively lower dimensionality compared with the original input. Subsequently, the decoder generates the target output based on the learned latent representation of multimodal data.[171] Additionally, the training of multimodal models requires extraordinary computational resources, leading to prohibitive costs in both the training and inference phases. At the architectural level, conventional serial computing architectures require analog-to-digital signal conversion prior to information processing, thereby imposing increased demands

on communication bandwidth and power consumption. Drawing inspiration from the parallel-processing capabilities of biological sensory systems and their energy-efficient characteristics, the development of brain-inspired neuromorphic chips composed of artificial synapses and neurons shows promise for achieving real-time multimodal signal fusion and energy-efficient processing. With advances in bionic design methodologies, cutting-edge manufacturing techniques, and AI innovations, future multimodal adaptive sensing systems are expected to exhibit enhanced intelligence, efficiency, and reliability. These advancements are poised to drive transformative developments across multiple domains, including humanoid robotics, neural prosthetics, machine vision, pilotless vehicles, and human–computer interaction systems.

Acknowledgements

G.G. and Y.Z. contributed equally to this study. S.-T.H. acknowledges financial support from the Hong Kong Research Grants Council, Young Collaborative Research Grant (C5001-24Y), Research Institute for Smart Energy, and Guangdong Provincial Department of Science and Technology (2024B1515040002). Y. Zhou acknowledges grants from RSC Sustainable Laboratories Grant (L24-8215098370), Guangdong Basic and Applied Basic Research Foundation (2023A1515012479), the Science and Technology Innovation Commission of Shenzhen (ICY|20220818100206013), RSC Researcher Collaborations Grant (C23-2422436283), State Key Laboratory of Radio Frequency Heterogeneous Integration (Independent Scientific Research Program No. 2024010), and NTUT-SZU Joint Research Program. This work was also supported by the National Natural Science Foundation of China (52373248), Guangdong Provincial Department of Science and Technology (2024A1515010006 and 2024A1515011718), Guangdong Basic and Applied Basic Research Foundation (2023A1515012479 and 2025A1515011274), and Science and Technology Innovation Commission of Shenzhen (JCYJ20230808105900001, JCYJ20220531102214032, and 20231123155543001).

Conflict of Interest

The authors declare no conflict of interest.

Keywords

bioinspired electronics, memristor, neuromorphic transistor, piezoelectric and triboelectric sensors, sensory adaptation

Received: March 20, 2025 Revised: June 23, 2025 Published online:

- [1] F. Zhou, Y. Chai, Nat. Electron. 2020, 3, 664.
- [2] T. P. Truong, H. T. Le, T. T. Nguyen, J. Phys. Conf. Ser. 2020, 1432, 012068.
- [3] S. Wang, C. Y. Wang, P. Wang, C. Wang, Z. A. Li, C. Pan, Y. Dai, A. Gao, C. Liu, J. Liu, H. Yang, X. Liu, B. Cheng, K. Chen, Z. Wang, K. Watanabe, T. Taniguchi, S. J. Liang, F. Miao, *Natl. Sci. Rev.* 2021, 8, nwaa172.
- [4] T. Y. Qu, Y. Sun, M. L. Chen, Z. B. Liu, Q. B. Zhu, B. W. Wang, T. Y. Zhao, C. Liu, J. Tan, S. Qiu, Q. W. Li, Z. Han, W. Wang, H. M. Cheng, D. M. Sun, Adv. Mater. 2020, 32, 1907288.

- [5] H. Tan, G. Liu, H. Yang, X. Yi, L. Pan, J. Shang, S. Long, M. Liu, Y. Wu, R. W. Li, ACS Nano 2017, 11, 11298.
- [6] F. Zhou, Z. Zhou, J. Chen, T. H. Choy, J. Wang, N. Zhang, Z. Lin, S. Yu, J. Kang, H. P. Wong, Y. Chai, Nat. Nanotechnol. 2019, 14, 776.
- [7] Y. Zhou, J. Fu, Z. Chen, F. Zhuge, Y. Wang, J. Yan, S. Ma, L. Xu, H. Yuan, M. Chan, X. Miao, Y. He, Y. Chai, *Nat. Electron.* 2023, 6, 870
- [8] Y. Chai, Nature 2020, 579, 32.
- [9] H. Tan, S. van Dijken, Nat. Electron. 2024, 7, 946.
- [10] S. Wang, X. Chen, C. Zhao, Y. Kong, B. Lin, Y. Wu, Z. Bi, Z. Xuan, T. Li, Y. Li, W. Zhang, E. Ma, Z. Wang, W. Ma, Nat. Electron. 2023, 6, 281.
- [11] L. Gu, S. Poddar, Y. Lin, Z. Long, D. Zhang, Q. Zhang, L. Shu, X. Qiu, M. Kam, A. Javey, Z. Fan, *Nature* 2020, 581, 278.
- [12] L. Mennel, J. Symonowicz, S. Wachter, D. K. Polyushkin, A. J. Molina-Mendoza, T. Mueller, *Nature* 2020, 579, 62.
- [13] B. Dang, T. Zhang, X. Wu, K. Liu, R. Huang, Y. Yang, Nat. Electron. 2024, 7, 991.
- [14] A. Dodda, D. Jayachandran, A. Pannone, N. Trainor, S. P. Stepanoff, M. A. Steves, S. S. Radhakrishnan, S. Bachu, C. W. Ordonez, J. R. Shallenberger, J. M. Redwing, K. L. Knappenberger, D. E. Wolfe, S. Das, Nat. Mater. 2022, 21, 1379.
- [15] J. Zha, S. Shi, A. Chaturvedi, H. Huang, P. Yang, Y. Yao, S. Li, Y. Xia, Z. Zhang, W. Wang, H. Wang, S. Wang, Z. Yuan, Z. Yang, Q. He, H. Tai, E. H. T. Teo, H. Yu, J. C. Ho, Z. Wang, H. Zhang, C. Tan, Adv. Mater. 2023, 35, 2211598.
- [16] F. Liao, F. Zhou, Y. Chai, J. Semicond. 2021, 42, 013105.
- [17] H. Tan, S. van Dijken, Nat. Commun. 2023, 14, 2169.
- [18] Y. Ni, J. Liu, H. Han, Q. Yu, L. Yang, Z. Xu, C. Jiang, L. Liu, W. Xu, Nat. Commun. 2024, 15, 3454.
- [19] Z. Zhang, S. Wang, C. Liu, R. Xie, W. Hu, P. Zhou, Nat. Nanotechnol. 2022, 17, 27.
- [20] C. Liu, H. Chen, S. Wang, Q. Liu, Y. Jiang, D. Zhang, M. Liu, P. Zhou, Nat. Nanotechnol. 2020, 15, 545.
- [21] J. J. Kim, H. Liu, A. Ousati Ashtiani, H. Jiang, Rep. Prog. Phys. 2020, 83, 047101.
- [22] H. Jiang, Nature 2020, 581, 264.
- [23] F. Li, S. Gao, Y. Lu, W. Asghar, J. Cao, C. Hu, H. Yang, Y. Wu, S. Li, J. Shang, M. Liao, Y. Liu, R. W. Li, Adv. Sci. 2021, 8, 2004208.
- [24] H. C. Ko, M. P. Stoykovich, J. Song, V. Malyarchuk, W. M. Choi, C. J. Yu, J. B. Geddes, 3rd, J. Xiao, S. Wang, Y. Huang, J. A. Rogers, *Nature* 2008, 454, 748.
- [25] M. S. Mannoor, Z. Jiang, T. James, Y. L. Kong, K. A. Malatesta, W. O. Soboyejo, N. Verma, D. H. Gracias, M. C. McAlpine, *Nano Lett.* 2013, 13, 2634.
- [26] S. B. Laughlin, J. Exp. Biol. 1989, 146, 39.
- [27] A. Nikolaev, K. M. Leung, B. Odermatt, L. Lagnado, *Nat. Neurosci.* 2013, 16, 934.
- [28] C. J. Whitmire, G. B. Stanley, Neuron 2016, 92, 298.
- [29] B. Wark, B. N. Lundstrom, A. Fairhall, Curr. Opin. Neurobiol. 2007, 17, 423.
- [30] Y. Tu, W. J. Rappel, Annu. Rev. Condens. Matter Phys. 2018, 9, 183.
- [31] M. Ramaswami, Neuron 2014, 82, 1216.
- [32] D. E. Koshland, A. Goldbeter, J. B. Stock, Science 1982, 217, 220.
- [33] J. Hao, P. Delmas, J. Neurosci. 2010, 30, 13384.
- [34] F. A. Dunn, M. J. Lankheet, F. Rieke, Nature 2007, 449, 603.
- [35] W. Ma, A. Trusina, H. El-Samad, W. A. Lim, C. Tang, Cell 2009, 138, 760.
- [36] G. Lan, P. Sartori, S. Neumann, V. Sourjik, Y. Tu, Nat. Phys. 2012, 8, 422.
- [37] Z. K. Esfahani, M. Tohidian, H. Zeijl, M. Kolahdouz, G. Zhang, IEEE Photonics J. 2017, 9, 2400213.
- [38] D. K. Polyushkin, S. Wachter, L. Mennel, M. Paur, M. Paliy, G. Iannaccone, G. Fiori, D. Neumaier, B. Canto, T. Mueller, Nat. Electron. 2020, 3, 486.

litions) on Wiley Online Library for rules of use; OA articles are governed by the applicable Creative Commons

www.advancedsciencenews.com



www.advmat.de

- [39] M. A. Mahowald, Vis. Inf. Process.: Neurons Chips 1991, 1473, 52.
- [40] P. Hasler, B. A. Minch, C. Diorio, IEEE Trans. Circ. Syst. II 2001, 48, 74.
- [41] Q. Xia, J. J. Yang, Nat. Mater. 2019, 18, 309.
- [42] S. J. Hong, Y. R. Lee, A. Bag, H. S. Kim, T. Q. Trung, M. J. Sultan, D. B. Moon, N. E. Lee, *Nat. Mater.* 2025.
- [43] S. Li, A. Liu, W. Qiu, Y. Wang, G. Liu, J. Liu, Y. Shi, Y. Li, J. Li, W. Cai, C. Park, M. Ye, W. Guo, ACS Nano 2024, 18, 4579.
- [44] J. Li, J. Yin, M. G. V. Wee, A. Chinnappan, S. Ramakrishna, Adv. Fiber Mater. 2023. 5, 1417.
- [45] E. Kar, P. Ghosh, S. Pratihar, M. Tavakoli, S. Sen, ACS Appl. Mater. Interfaces 2023, 15, 20372.
- [46] S. Zhu, T. Xie, Z. Lv, Y. B. Leng, Y. Q. Zhang, R. Xu, J. Qin, Y. Zhou, V. A. L. Roy, S. T. Han, Adv. Mater. 2024, 36, 2301986.
- [47] Z. Hu, Y. Hu, L. Su, X. Fang, Laser Photonics Rev. 2024, 18, 2301364.
- [48] W. Ci, W. Xue, P. Wang, W. Yin, X. Wang, L. Shi, P. Zhou, X. Xu, Adv. Funct. Mater. 2024, 34, 2305822.
- [49] S. Duan, X. Zhang, Y. Xi, D. Liu, X. Zhang, C. Li, L. Jiang, L. Li, H. Chen, X. Ren, W. Hu, Adv. Mater. 2024, 36, 2405030.
- [50] J. Kuang, K. Liu, M. Liu, M. Shao, M. Zhu, G. Liu, W. Wen, J. Chen, M. Qin, Z. Pan, Z. Zhao, Y. Liu, Y. Guo, Adv. Funct. Mater. 2023, 33, 2209502
- [51] C. Jin, W. Liu, Y. Xu, Y. Huang, Y. Nie, X. Shi, G. Zhang, P. He, J. Zhang, H. Cao, J. Sun, J. Yang, Nano Lett. 2022, 22, 3372.
- [52] Z. Gao, X. Ju, H. Zhang, X. Liu, H. Chen, W. Li, H. Zhang, L. Liang, H. Cao, Adv. Funct. Mater. 2023, 33, 2305959.
- [53] Y. Wang, J. Hua, X. He, S. Liu, J. Li, H. Zhang, J. Fu, L. Wang, W. Li, M. Yi, L. Xie, W. Huang, H. Ling, Adv. Funct. Mater. 2024, 35, 2414546.
- [54] D. Purves, G. J. Augustine, D. Fitzpatrick, W. C. Hall, A. S. LaMantia, R. D. Mooney, M. L. Platt, L. E. White, *Neuroscience*, Oxford University Press, New York 2018.
- [55] P. Delmas, J. Hao, L. Rodat-Despoix, Nat. Rev. Neurosci. 2011, 12, 139.
- [56] C. L. Stanfield, Principles of Human Physiology, Pearson, Boston 2017.
- [57] I. M. Dozmorov, D. Dresser, Int. J. Biomed. Sci. 2010, 6, 167.
- [58] M. Mendelson, W. R. Loewenstein, Science 1964, 144, 554.
- [59] L. S. Costanzo, Physiology, Elsevier, Philadelphia, PA 2018.
- [60] E. A. Lumpkin, M. J. Caterina, Nature 2007, 445, 858.
- [61] R. S. Johansson, J. R. Flanagan, Nat. Rev. Neurosci. 2009, 10, 345.
- [62] B. Wark, A. Fairhall, F. Rieke, Neuron 2009, 61, 750.
- [63] N. Gupta, M. Stopfer, Curr. Opin. Neurobiol. 2011, 21, 768.
- [64] P. Sartori, Y. Tu, Phys. Rev. Lett. 2015, 115, 118102.
- [65] S. Musall, W. Behrens, J. M. Mayrhofer, B. Weber, F. Helmchen, F. Haiss, Nat. Neurosci. 2014, 17, 1567.
- [66] M. Wang, Y. Luo, T. Wang, C. Wan, L. Pan, S. Pan, K. He, A. Neo, X. Chen, Adv. Mater. 2020, 33, 2003014.
- [67] Y. Kim, A. Chortos, W. Xu, Y. Liu, J. Y. Oh, D. Son, J. Kang, A. M. Foudeh, C. Zhu, Y. Lee, S. Niu, J. Liu, R. Pfattner, Z. Bao, T.-W. Lee, *Science* 2018, 360, 998.
- [68] E. R. Kandel, J. H. Schwartz, T. M. Jessell, S. A. Siegelbaum, A. J. Hudspeth, Principles of Neural Science, McGraw Hill, New York 2013.
- [69] V. E. Abraira, D. D. Ginty, Neuron 2013, 79, 618.
- [70] A. I. Weber, H. P. Saal, J. D. Lieber, J. W. Cheng, L. R. Manfredi, J. F. Dammann, III, S. J. Bensmaia, Proc. Natl. Acad. Sci. U.S.A. 2013, 110, 17107.
- [71] P. Jenmalm, I. Birznieks, A. W. Goodwin, R. S. Johansson, Eur. J. Neurosci. 2003, 18, 164.
- [72] M. R. Chambers, K. H. Andres, M. v. Duering, A. Iggo, Q. J. Exp. Physiol. Cogn. Med. Sci. 1972, 57, 417.
- [73] K. O. Johnson, Curr. Opin. Neurobiol. 2001, 11, 455.
- [74] M. A. Srinivasan, J. M. Whitehouse, R. H. LaMotte, J. Neurophysiol. 1990, 63, 1323.

- [75] J. Scheibert, S. Leurent, A. Prevost, G. Debrégeas, *Science* 2009, 323, 1503.
- [76] S. Chen, Z. Lou, D. Chen, G. Shen, Adv. Mater. 2018, 30, 1705400.
- [77] R. Q. Quiroga, L. Reddy, G. Kreiman, C. Koch, I. Fried, *Nature* 2005, 435, 1102.
- [78] I. G. Sligte, A. R. Vandenbroucke, H. S. Scholte, V. A. Lamme, Front. Psychol. 2010, 1, 175.
- [79] D. C. D. Pocock, Trans. Inst. Br. Geogr. 1981, 6, 385.
- [80] S. Mathôt, J. Cogn. 2018, 1, 16.
- [81] T. Gollisch, M. Meister, Neuron 2010, 65, 150.
- [82] V. I. Govardovskii, P. D. Calvert, V. Y. Arshavsky, J. Gen. Physiol. 2000, 116, 791.
- [83] E. N. Pugh, S. Nikonov, T. D. Lamb, Curr. Opin. Neurobiol. 1999, 9, 410
- [84] A. Darmont, High Dynamic Range Imaging: Sensors and Architectures, SPIE Press, Bellingham 2019.
- [85] H. Seetzen, W. Heidrich, W. Stuerzlinger, G. Ward, L. Whitehead, M. Trentacoste, A. Ghosh, A. Vorozcovs, ACM Trans. Graph. 2004, 23, 760.
- [86] J. G. Nicholls, A. R. Martin, P. A. Fuchs, D. A. Brown, M. E. Diamond, D. A. Weisblat, From Neuron to Brain, Sinauer Associates, Sunderland, MA 2012.
- [87] D. Jameson, L. M. Hurvich, Handbook of Sensory Physiology, SpringerVerlag, Berlin 1972.
- [88] A. Morshedian, G. L. Fain, J. Physiol. 2017, 595, 4947.
- [89] G. L. Fain, H. R. Matthews, M. C. Cornwall, Y. Koutalos, *Physiol. Rev.* 2001, 81, 117.
- [90] A. J. Ricci, R. Fettiplace, J. Physiol. 1997, 501, 111.
- [91] B. D. B. Willmore, A. J. King, Physiol. Rev. 2023, 103, 1025.
- [92] J. E. Cometto-Muñiz, W. S. Cain, Olfactory Adaptation, Marcel Dekker. New York 1995.
- [93] J. F. Gent, D. H. McBurney, Percept. Psychophysics 1978, 23, 171.
- [94] G. Gong, Y. Zhou, Z. Xiong, T. Sun, H. Li, Q. Li, W. Zhao, G. Zhang, Y. Zhai, Z. Lv, H. Tan, Y. Zhou, S. T. Han, Adv. Mater. 2024, 36, 2409844.
- [95] F. Liao, Z. Zhou, B. J. Kim, J. Chen, J. Wang, T. Wan, Y. Zhou, A. T. Hoang, C. Wang, J. Kang, J. H. Ahn, Y. Chai, *Nat. Electron.* 2022, 5, 84
- [96] J. Shi, Y. Lin, Z. Wang, X. Shan, Y. Tao, X. Zhao, H. Xu, Y. Liu, Adv. Mater. 2024, 36, 2314156.
- [97] H. Shen, Z. He, W. Jin, L. Xiang, W. Zhao, C. Di, D. Zhu, Adv. Mater. 2019, 31, 1905018.
- [98] M. Hollins, S. R. Risner, Percept. Psychophys. 2000, 62, 695.
- [99] S. Chun, I. Hwang, W. Son, J. H. Chang, W. Park, Nanoscale 2018, 10, 10545.
- [100] S. Pyo, J. Lee, K. Bae, S. Sim, J. Kim, Adv. Mater. 2021, 33, 2005902.
- [101] A. Chortos, J. Liu, Z. Bao, Nat. Mater. 2016, 15, 937.
- [102] W. Deng, Y. Zhou, A. Libanori, G. Chen, W. Yang, J. Chen, Chem. Soc. Rev. 2022, 51, 3380.
- [103] T. Vijayakanth, S. Shankar, G. Finkelstein-Zuta, S. Rencus-Lazar, S. Gilead, E. Gazit, Chem. Soc. Rev. 2023, 52, 6191.
- [104] J. Zhang, H. Yao, J. Mo, S. Chen, Y. Xie, S. Ma, R. Chen, T. Luo, W. Ling, L. Qin, Z. Wang, W. Zhou, Nat. Commun. 2022, 13, 5076.
- [105] J. Wang, J. Jiang, C. Zhang, M. Sun, S. Han, R. Zhang, N. Liang, D. Sun, H. Liu, Nano Energy 2020, 76, 105050.
- [106] W. Lin, B. Wang, G. Peng, Y. Shan, H. Hu, Z. Yang, Adv. Sci. 2021, 8, 2002817.
- [107] Y. Qiu, F. Wang, Z. Zhang, K. Shi, Y. Song, J. Lu, M. Xu, M. Qian, W. Zhang, J. Wu, Z. Zhang, H. Chai, A. Liu, H. Jiang, H. Wu, Sci. Adv. 2024, 10, adp0348.
- [108] K. Y. Chun, Y. J. Son, E. S. Jeon, S. Lee, C. S. Han, Adv. Mater. 2018, 30, 1706299.
- [109] P. Zhu, Y. Wang, Y. Wang, H. Mao, Q. Zhang, Y. Deng, Adv. Energy Mater. 2020, 10, 2001945.



www.advmat.de

- [110] J. Park, M. Kim, Y. Lee, H. S. Lee, H. Ko, Sci. Adv. 2015, 1, 1500661.
- [111] T. Cheng, J. Shao, Z. L. Wang, Nat. Rev. Methods Prim. 2023, 3, 39.
- [112] S. Duan, H. Zhang, L. Liu, Y. Lin, F. Zhao, P. Chen, S. Cao, K. Zhou, C. Gao, Z. Liu, Q. Shi, C. Lee, J. Wu, Mater. Today 2024, 80, 450.
- [113] J. Luo, W. Gao, Z. L. Wang, Adv. Mater. 2021, 33, 2004178.
- [114] A. A. Mathew, A. Chandrasekhar, S. Vivekanandan, *Nano Energy* 2021, 80, 105566.
- [115] J. Huang, X. Fu, G. Liu, S. Xu, X. Li, C. Zhang, L. Jiang, Nano Energy 2019, 62, 638.
- [116] J. Yu, X. Hou, M. Cui, S. Zhang, J. He, W. Geng, J. Mu, X. Chou, Nano Energy 2019, 64, 103923.
- [117] X. Qu, Z. Liu, P. Tan, C. Wang, Y. Liu, H. Feng, D. Luo, Z. Li, Z. L. Wang, Sci. Adv. 2022, 8, abq2521.
- [118] X. Wu, J. Zhu, J. W. Evans, A. C. Arias, Adv. Mater. 2020, 32, 2005970
- [119] Y. Wang, H. Wu, L. Xu, H. Zhang, Y. Yang, Z. L. Wang, Sci. Adv. 2020, 6, abb9083.
- [120] M. Vasilopoulou, A. R. B. M. Yusoff, Y. Chai, M. A. Kourtis, T. Matsushima, N. Gasparini, R. Du, F. Gao, M. K. Nazeeruddin, T. D. Anthopoulos, Y. Y. Noh, Nat. Electron. 2023, 6, 949.
- [121] H. Tan, Y. Zhou, Q. Tao, J. Rosen, S. van Dijken, Nat. Commun. 2021, 12. 1120.
- [122] T. Jiang, Y. Wang, Y. Zheng, L. Wang, X. He, L. Li, Y. Deng, H. Dong, H. Tian, Y. Geng, L. Xie, Y. Lei, H. Ling, D. Ji, W. Hu, *Nat. Commun.* 2023, 14, 2281.
- [123] Y. Liu, D. Liu, C. Gao, X. Zhang, R. Yu, X. Wang, E. Li, Y. Hu, T. Guo, H. Chen, Nat. Commun. 2022, 13, 7917.
- [124] P. Y. Huang, B. Y. Jiang, H. J. Chen, J. Y. Xu, K. Wang, C. Y. Zhu, X. Y. Hu, D. Li, L. Zhen, F. C. Zhou, J. K. Qin, C. Y. Xu, *Nat. Commun.* 2023, 14, 6736.
- [125] I. J. Kim, M. K. Kim, J. S. Lee, Nat. Commun. 2023, 14, 504.
- [126] H. Tan, G. Liu, X. Zhu, H. Yang, B. Chen, X. Chen, J. Shang, W. D. Lu, Y. Wu, R. W. Li, Adv. Mater. 2015, 27, 2797.
- [127] K. Zhu, S. Pazos, F. Aguirre, Y. Shen, Y. Yuan, W. Zheng, O. Alharbi, M. A. Villena, B. Fang, X. Li, A. Milozzi, M. Farronato, M. M. Rojo, T. Wang, R. Li, H. Fariborzi, J. B. Roldan, G. Benstetter, X. Zhang, H. N. Alshareef, T. Grasser, H. Wu, D. Ielmini, M. Lanza, *Nature* 2023, 618, 57
- [128] R. Y. Sun, Z. Y. Hou, Q. Chen, B. X. Zhu, C. Y. Zhu, P. Y. Huang, Z. H. Hu, L. Zhen, F. C. Zhou, C. Y. Xu, J. K. Qin, Adv. Mater. 2025, 37, 2409017.
- [129] M. Lanza, A. Sebastian, W. D. Lu, M. L. Gallo, M. F. Chang, D. Akinwande, F. M. Puglisi, H. N. Alshareef, M. Liu, J. B. Roldan, Science 2022, 376, abj9979.
- [130] Y. Park, J. S. Lee, ACS Nano 2017, 11, 8962.
- [131] S. H. Jo, T. Chang, I. Ebong, B. B. Bhadviya, P. Mazumder, W. Lu, Nano Lett. 2010, 10, 1297.
- [132] J. J. Yang, D. B. Strukov, D. R. Stewart, Nat. Nanotechnol. 2013, 8, 13.
- [133] M. Lanza, S. Pazos, F. Aguirre, A. Sebastian, M. L. Gallo, S. M. Alam, S. Ikegawa, J. J. Yang, E. Vianello, M. F. Chang, G. Molas, I. Naveh, D. Ielmini, M. Liu, J. B. Roldan, *Nature* 2025, 640, 613.
- [134] Z. Xie, S. Gao, X. Ye, H. Yang, G. Gong, Y. Lu, J. Ye, G. Liu, R. W. Li, Phys. Chem. Chem. Phys. 2020, 22, 26322.
- [135] I. J. Kim, J. S. Lee, Adv. Mater. 2023, 35, 2206864.
- [136] M. A. Zidan, J. P. Strachan, W. D. Lu, Nat. Electron. 2018, 1, 22.
- [137] X. Liu, C. Sun, X. Ye, X. Zhu, C. Hu, H. Tan, S. He, M. Shao, R. W. Li, Adv. Mater. 2024, 36, 2311472.
- [138] G. Gong, C. Wu, P. Hu, Y. Li, N. Kwon, C. Liu, Curr. Appl. Phys. 2016, 16, 980
- [139] H. Tan, Q. Tao, I. Pande, S. Majumdar, F. Liu, Y. Zhou, P. O. Å. Persson, J. Rosen, S. Dijken, Nat. Commun. 2020, 11, 1369.

- [140] C. Jiang, J. Liu, Y. Ni, S. Qu, L. Liu, Y. Li, L. Yang, W. Xu, Nat. Commun. 2023, 14, 1344.
- [141] G. Zhang, J. Qin, Y. Zhang, G. Gong, Z. Y. Xiong, X. Ma, Z. Lv, Y. Zhou, S. T. Han, Adv. Funct. Mater. 2023, 33, 2302929.
- [142] H. X. Li, Q. X. Li, F. Z. Li, J. P. Liu, G. D. Gong, Y. Q. Zhang, Y. B. Leng, T. Sun, Y. Zhou, S. T. Han, Adv. Mater. 2024, 36, 2308153.
- [143] G. Zhou, J. Li, Q. Song, L. Wang, Z. Ren, B. Sun, X. Hu, W. Wang, G. Xu, X. Chen, L. Cheng, F. Zhou, S. Duan, *Nat. Commun.* 2023, 14, 8489.
- [144] Z. Wu, J. Lu, T. Shi, X. Zhao, X. Zhang, Y. Yang, F. Wu, Y. Li, Q. Liu, M. Liu, Adv. Mater. 2020, 32, 2004398.
- [145] Y. Wang, Y. Gong, S. Huang, X. Xing, Z. Lv, J. Wang, J. Q. Yang, G. Zhang, Y. Zhou, S. T. Han, Nat. Commun. 2021, 12, 5979.
- [146] Y. G. Song, J. M. Suh, J. Y. Park, J. E. Kim, S. Y. Chun, J. U. Kwon, H. Lee, H. W. Jang, S. Kim, C. Y. Kang, J. H. Yoon, Adv. Sci. 2022, 9, 2103484.
- [147] Y. J. Du, J. Yang, Z. Lv, Y. Zhai, Z. Yi, Y. Xie, M. L. Zheng, X. Ma, G. Gong, Y. Wang, Y. Zhou, S. T. Han, Adv. Funct. Mater. 2025, 2500953.
- [148] S. Gao, G. Liu, H. Yang, C. Hu, Q. Chen, G. Gong, W. Xue, X. Yi, J. Shang, R. W. Li, ACS Nano 2019, 13, 2634.
- [149] Q. Chen, Y. Zhang, S. Liu, T. Han, X. Chen, Y. Xu, Z. Meng, G. Zhang, X. Zheng, J. Zhao, G. Cao, G. Liu, Adv. Intell. Syst. 2020, 2, 2000122.
- [150] W. Liu, X. Yang, Z. Wang, Y. Li, J. Li, Q. Feng, X. Xie, W. Xin, H. Xu, Y. Liu, Light Sci. Appl. 2023, 12, 180.
- [151] X. Geng, L. Hu, F. Zhuge, X. Wei, Adv. Intell. Syst. 2022, 4, 2200019.
- [152] Z. Xie, X. Zhu, W. Wang, Z. Guo, Y. Zhang, H. Liu, C. Sun, M. Tang, S. Gao, R. W. Li, Adv. Electron. Mater. 2022, 8, 2200334.
- [153] L. Hu, Z. Li, J. Shao, P. Cheng, J. Wang, A. V. Vasilakos, L. Zhang, Y. Chai, Z. Ye, F. Zhuge, *Nano Lett.* 2024, 24, 10865.
- [154] A. Shaban, S. S. Bezugam, M. Suri, Nat. Commun. 2021, 12, 4234.
- [155] S. S. Radhakrishnan, S. Chakrabarti, D. Sen, M. Das, T. F. Schranghamer, A. Sebastian, S. Das, Adv. Mater. 2022, 34, 2202535.
- [156] Y. Cai, F. Wang, X. Wang, S. Li, Y. Wang, J. Yang, T. Yan, X. Zhan, F. Wang, R. Cheng, J. He, Z. Wang, Adv. Funct. Mater. 2022, 33, 2212917.
- [157] B. M. Dhar, R. Özgün, T. Dawidczyk, A. Andreou, H. E. Katz, *Mater. Sci. Eng. R Rep.* 2011, 72, 49.
- [158] D. Xie, L. Wei, M. Xie, L. Jiang, J. Yang, J. He, J. Jiang, Adv. Funct. Mater. 2021, 31, 2010655.
- [159] D. Xie, G. Gao, B. Tian, Z. Shu, H. Duan, W. W. Zhao, J. He, J. Jiang, Adv. Mater. 2023, 35, 2212118.
- [160] M. Zhang, Z. Chi, G. Wang, Z. Fan, H. Wu, P. Yang, J. Yang, P. Yan, Z. Sun, Adv. Mater. 2022, 34, 2205679.
- [161] L. Shi, K. Shi, Z. C. Zhang, Y. Li, F. D. Wang, S. H. Si, Z. B. Liu, T. B. Lu, X. D. Chen, J. Zhang, SmartMat. 2024, 5, 1285.
- [162] Z. He, H. Shen, D. Ye, L. Xiang, W. Zhao, J. Ding, F. Zhang, C. Di, D. Zhu, Nat. Electron. 2021, 4, 522.
- [163] S. Hong, S. H. Choi, J. Park, H. Yoo, J. Y. Oh, E. Hwang, D. H. Yoon, S. Kim, ACS Nano 2020, 14, 9796.
- [164] S. M. Kwon, S. W. Cho, M. Kim, J. S. Heo, Y. H. Kim, S. K. Park, Adv. Mater. 2019, 31, 1906433.
- [165] A. Bag, G. Ghosh, M. J. Sultan, H. H. Chouhdry, S. J. Hong, T. Q. Trung, G. Y. Kang, N. E. Lee, Adv. Mater. 2024, 2403150.
- [166] Z. He, D. Ye, L. Liu, C. Di, D. Zhu, Mater. Horiz. 2022, 9, 147.
- [167] G. Gong, S. Gao, Z. Xie, X. Ye, Y. Lu, H. Yang, X. Zhu, R. W. Li, Nanoscale 2021, 13, 1029.
- [168] S. Wang, S. Gao, C. Tang, E. Occhipinti, C. Li, S. Wang, J. Wang, H. Zhao, G. Hu, A. Nathan, R. Dahiya, L. G. Occhipinti, *Nat. Commun.* 2024, 15, 4671.
- [169] S. Chun, J. S. Kim, Y. Yoo, Y. Choi, S. J. Jung, D. Jang, G. Lee, K. Song, K. S. Nam, I. Youn, D. Son, C. Pang, Y. Jeong, H. Jung, Y. J. Kim, B. D. Choi, J. Kim, S. P. Kim, W. Park, S. Park, *Nat. Electron.* 2021, 4, 429.

- [170] T. D. Do, T. Q. Trung, A. L. Mong, H. Q. Huynh, D. Lee, S. J. Hong, D. T. Vu, M. Kim, N. E. Lee, ACS Appl. Mater. Interfaces 2024, 16, 20813.
- [171] K. Mahato, T. Saha, S. Ding, S. S. Sandhu, A. Y. Chang, J. Wang, Nat. Electron. 2024, 7, 735.
- [172] A. Roy, R. Afshari, S. Jain, Y. Zheng, M. H. Lin, S. Zenkar, J. Yin, J. Chen, N. A. Peppas, N. Annabi, Chem. Soc. Rev. 2025, 54, 2595.
- [173] J. Xiong, L. Wang, F. Liang, M. Li, Y. Yabuta, M. A. Iqbal, G. Mayakrishnan, J. Shi, I. S. Kim, Adv. Fiber Mater. 2024, 6, 1212.
- [174] Y. Fang, J. Xu, X. Xiao, Y. Zou, X. Zhao, Y. Zhou, J. Chen, *Adv. Mater.* **2022**, *34*, 2200252.
- [175] F. Wen, Z. Zhang, T. He, C. Lee, Nat. Commun. 2021, 12, 5378.
- [176] Y. Pang, X. Xu, S. Chen, Y. Fang, X. Shi, Y. Deng, Z. L. Wang, C. Cao, Nano Energy 2022, 96, 107137.
- [177] A. Bag, N. E. Lee, Adv. Mater. Technol. 2021, 6, 2000883.
- [178] H. He, C. Dong, Y. Fu, W. Han, T. Zhao, L. Xing, X. Xue, Sensor Actuat. B-Chem. 2018, 267, 392.
- [179] D. Maier, E. Laubender, A. Basavanna, S. Schumann, F. Güder, G. A. Urban, C. Dincer, ACS Sens. 2019, 4, 2945.
- [180] Z. Wang, T. Wan, S. Ma, Y. Chai, Nat. Nanotechnol. 2024, 19, 919.
- [181] J. Chen, Z. Zhou, B. J. Kim, Y. Zhou, Z. Wang, T. Wan, J. Yan, J. Kang, J. H. Ahn, Y. Chai, Nat. Nanotechnol. 2023, 18, 882.
- [182] L. Li, S. Li, W. Wang, J. Zhang, Y. Sun, Q. Deng, T. Zheng, J. Lu, W. Gao, M. Yang, H. Wang, Y. Pan, X. Liu, Y. Yang, J. Li, N. Huo, Nat. Commun. 2024, 15, 6261.

- [183] C. Wang, Y. Bian, K. Liu, M. Qin, F. Zhang, M. Zhu, W. Shi, M. Shao, S. Shang, J. Hong, Z. Zhu, Z. Zhao, Y. Liu, Y. Guo, *Nat. Commun.* 2024, 15, 3123.
- [184] J. C. Corbo, Dev. Biol. 2021, 475, 145.
- [185] J. M. Enright, M. B. Toomey, S. Y. Sato, S. E. Temple, J. R. Allen, R. Fujiwara, V. M. Kramlinger, L. D. Nagy, K. M. Johnson, Y. Xiao, M. J. How, S. L. Johnson, N. W. Roberts, V. J. Kefalov, F. P. Guengerich, J. C. Corbo, Curr. Biol. 2015, 25, 3048
- [186] B. Ouyang, J. Wang, G. Zeng, J. Yan, Y. Zhou, X. Jiang, B. Shao, Y. Chai, Nat. Electron. 2024, 7, 705.
- [187] Y. Tan, H. Hao, Y. Chen, Y. Kang, T. Xu, C. Li, X. Xie, T. Jiang, Adv. Mater. 2022, 34, 2206816.
- [188] S. E. Ng, N. Yantara, N. A. Tu, E. Erdenebileg, P. W. F. Li, D. Sharma, Y. M. Lam, S. Mhaisalkar, A. Basu, A. Chattopadhyay, N. Mathews, Adv. Mater. 2024, 36, 2406568.
- [189] X. Yan, L. Zhang, Y. Yang, Z. Zhou, J. Zhao, Y. Zhang, Q. Liu, J. Chen, J. Mater. Chem. C 2017, 5, 11046.
- [190] X. Yan, Y. Pei, H. Chen, J. Zhao, Z. Zhou, H. Wang, L. Zhang, J. Wang, X. Li, C. Qin, G. Wang, Z. Xiao, Q. Zhao, K. Wang, H. Li, D. Ren, Q. Liu, H. Zhou, J. Chen, P. Zhou, Adv. Mater. 2019, 31, 1805284.
- [191] J. Zhu, X. Zhang, R. Wang, M. Wang, P. Chen, L. Cheng, Z. Wu, Y. Wang, Q. Liu, M. Liu, Adv. Mater. 2022, 34, 2200481.
- [192] F. Zhao, C. Zhang, B. Geng, ACM Comput. Surv. 2024, 56, 216.



Guodong Gong is currently a postdoctoral fellow at the Shenzhen University. He received Ph.D. in Materials Physics and Chemistry from the University of the Chinese Academy of Sciences in 2022. His research interests include fabrication of nanoscale optoelectronic devices and their applications in intelligent sensing and neuromorphic computing.



You Zhou received his bachelor's degree in microelectronics science and engineering from Shenzhen University. He is currently a postgraduate student at the Institute of Microscale Optoelectronics at Shenzhen University. His research interests include memristors and optoelectronic devices.

15214095, 0, Downloaded from https://advanced.onlinelibrary.wiley.com/doi/10.1002/adma.202505420 by HONG KONG POLYTECHNIC UNIVERSITY HU NG HOM, Wiley Online Library on [26092025]. See the Terms

and-conditions) on Wiley Online Library for rules of use; OA articles are governed by the applicable Creative Commons License



Su-Ting Han is currently an associate professor in the Department of Applied Biology and Chemical Technology at Hong Kong Polytechnic University. She received Ph.D. in Physics and Materials Science from the City University of Hong Kong in 2014 and became a postdoctoral researcher. She joined Shenzhen University in 2016 and was promoted to full professor (tenured) in 2021 and then to distinguished professor in 2022. She was a visiting professor in the Department of Electrical Engineering and Computer Science at the University of Michigan, US, in 2019. Her research interests include flash memories, memristors, neuromorphic devices, and in-memory computing systems.